

Nuclear effects in the Drell-Yan process at very high energies

B.Z. Kopeliovich^{a,b,c}, J. Raufeisen^d, A.V. Tarasov^{a,b,c}, and M.B. Johnson^d

^aMax-Planck Institut für Kernphysik, Postfach 103980, 69029 Heidelberg, Germany

^bInstitut für Theoretische Physik der Universität, 93040 Regensburg, Germany

^cJoint Institute for Nuclear Research, Dubna, 141980 Moscow Region, Russia

^dLos Alamos National Laboratory, MS H846, Los Alamos, NM 87545, USA

Abstract

We study Drell-Yan (DY) dilepton production in proton(deuterium)-nucleus and in nucleus-nucleus collisions within the light-cone color dipole formalism. This approach is especially suitable for predicting nuclear effects in the DY cross section for heavy ion collisions, as it provides the impact parameter dependence of nuclear shadowing and transverse momentum broadening, quantities that are not available from the standard parton model. For $p(D) + A$ collisions we calculate nuclear shadowing and investigate nuclear modification of the DY transverse momentum distribution at RHIC and LHC for kinematics corresponding to coherence length much longer than the nuclear size. Calculations are performed separately for transversely and longitudinally polarized DY photons, and predictions are presented for the dilepton angular distribution. Furthermore, we calculate nuclear broadening of the mean transverse momentum squared of DY dileptons as function of the nuclear mass number and energy. We also predict nuclear effects for the cross section of the DY process in heavy ion collisions. We found a substantial nuclear shadowing for valence quarks, stronger than for the sea.

PACS: 13.85.Qk; 24.85.+p; 24.70.+s

Keywords: Drell-Yan process; nuclear shadowing; heavy-ion collisions

1 Introduction

The cross section for the Drell-Yan (DY) process at the energies of the SPS suggests rather weak nuclear effects, if any at all (although measurements at small Feynman x_F are the only data available). However, the fixed target experiment E772 at Fermilab at 800 GeV [1] shows a sizable nuclear suppression at large x_F . Although this suppression results from a complicated interplay between energy loss and shadowing [2, 3], shadowing effects are expected to be much stronger and span the entire range of x_F at the energies of the Relativistic Heavy Ion Collider (RHIC) and the Large Hadron Collider (LHC).

Relying on the standard parton model for proton-nucleus collisions, one can predict the DY cross section integrated over transverse momentum employing QCD factorization and data for the nuclear structure functions measured in deep-inelastic scattering (DIS)¹. However, no reliable means to calculate nuclear effects in the transverse momentum distribution within the parton model is available. Therefore, one has to parameterize nuclear broadening according to Brownian motion in the plane of transverse momentum and fit to data (see [6] for a review). Perhaps, this situation will be improved by higher-twist factorization theorems [7] in the future.

Moreover, parton model predictions are doubtful even for the integrated DY cross section in nucleus-nucleus collisions. Indeed, compared to pA collisions, this case requires knowledge of the impact parameter dependence of nuclear shadowing and, of course, the introduction of an additional integration over the impact parameter [see Eq. (47)]. Neither DIS nor the DY reaction on nuclei provides the information needed for this. In principle one can access such information relying, for instance, on knowledge of the number of so-called gray tracks and using simple cascade models. However, this possibility has never been realized either for the DIS or the DY process. In view of this problem, it might be tempting to assume, as in a recent analysis [8], that nuclear shadowing is independent of impact parameter. Clearly, this cannot be correct and can lead to unphysical results such as a DY cross section in heavy ion collisions independent of centrality. It is known, however, for many processes, that peripheral collisions are similar to the free NN interaction, while central collisions should manifest the strongest nuclear effects.

In this paper we calculate nuclear shadowing for the DY cross section using the light-cone (LC) dipole approach suggested in [9]. This approach formulates the DY reaction in the rest frame of the target, which allows one to overcome these problems in a simple way by taking advantage of the description of the DY process as bremsstrahlung of a heavy photon from a beam quark that subsequently decays into the lepton pair as in fig. 1. Although this looks very different from the more familiar DY mechanism [10], which interprets the DY reaction as quark-antiquark annihilation, it is known that the space-time interpretation of high-energy reactions is not Lorentz invariant and depends on the frame of reference. Indeed, it is only in a fast-moving frame where Feynman's picture of the colliding particles

¹The analysis of data [4] based on the DGLAP evolution equations still neglects effects of saturation [5] that should be important once shadowing sets in. Additionally, no data for DIS on nuclei are available for small Bjorken x relevant for LHC. Existing data for DIS and DY are not sensitive to the amount of gluon shadowing, which had to be parameterized ad hoc in [4].

as bundles of non-interacting partons with no (or small) transverse momenta is valid and the DY reaction can be formulated consistently in terms of the parton density of the proton (or nucleus).

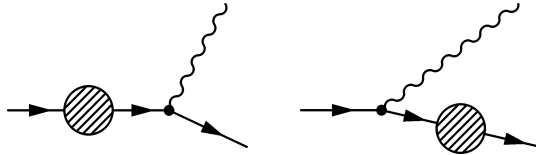


Figure 1: *In the target rest frame, DY dilepton production looks like bremsstrahlung. A quark or an anti-quark from the projectile hadron scatters off the target color field (denoted by the shaded circles) and radiates a massive photon, which subsequently decays into the lepton pair. The photon decay is not shown. The photon can be radiated before or after the quark scatters.*

In the target rest frame, a quark of the incident hadron fluctuates into a state that contains a massive photon (dilepton) and a quark. Interaction with the target breaks down the coherence of the fluctuation and the γ^* is freed. Correspondingly, the cross section of the process $qp \rightarrow \gamma^* X$ has a factorized form [9, 11, 12, 13, 14],

$$\frac{d\sigma(qp \rightarrow \gamma^* X)}{d\ln \alpha} = \int d^2 \rho |\Psi_{\gamma^* q}(\alpha, \rho)|^2 \sigma_{q\bar{q}}^N(\alpha\rho, x_2) . \quad (1)$$

where $\Psi_{\gamma^* q}(\alpha, \rho)$ is the LC distribution amplitude in Eqs. (B.2) or (B.3) for having a quark-photon (transversely or longitudinally polarized) fluctuation with transverse separation $\vec{\rho}$ and relative fractions α and $1 - \alpha$ of light-cone momenta carried by the photon and quark, respectively. For the DY reaction in pp -scattering, the dipole cross section needed in (1) is the same $\sigma_{q\bar{q}}^N$ as in DIS off a proton ². Note, that in the two graphs for bremsstrahlung, fig. 1, the quark scatters at different impact parameters, depending on whether it scatters when in the $|\gamma^* q\rangle$ -state (right) or not (left). This leads to the appearance of the dipole cross section $\sigma_{q\bar{q}}^N(\alpha\rho, x_2)$ in (1), although there is actually no physical dipole in this process [9, 13]. The light-cone Fock-state formulation of QCD is discussed in detail in the recent review [15].

We use standard kinematical variables,

$$x_1 = \frac{2P_2 \cdot q}{s} \quad , \quad x_2 = \frac{2P_1 \cdot q}{s} , \quad (2)$$

with $x_1 - x_2 = x_F$ and $x_1 x_2 = (M^2 + q_T^2)/s$, where P_1 , P_2 and q are the four-momenta of the beam, target and the virtual photon, respectively; $M^2 = q^2$ and \vec{q}_T are the dilepton invariant mass squared and transverse momentum, respectively; $s = (P_1 + P_2)^2$.

The frame dependence of the space-time interpretation of the DY process can be illustrated by the different meanings of x_1 in different reference frames: it is well known that in

²This can be proven in leading-log order or otherwise justified by referring to QCD factorization.

the standard picture of DY [10], x_1 is the momentum fraction of the projectile quark annihilating with the target antiquark. However, evaluating the scalar product (2) in the target rest frame shows that the projectile quark carries momentum fraction $x = x_1/\alpha > x_1$ of its parent hadron and, correspondingly, x_1 is the momentum fraction of the proton taken away by the photon. This is not a contradiction, since the projectile quarks in the two reference frames are different particles.

In the case of a pA -scattering, one has to distinguish between two limiting kinematical regimes for the DY reaction. On the one hand, there is the regime of short coherence time t_c , which can be interpreted as the mean fluctuation lifetime. If t_c is much shorter than the mean internucleon separation no effect of coherence (shadowing) is expected. On the other hand, in the regime of long coherence time compared to the nuclear radius, $t_c \gg R_A$, interference of the multiple interaction amplitudes with bound nucleons will affect the probability of breaking down the coherence of the fluctuation and releasing the dilepton on mass shell, i.e. shadowing (sometimes antishadowing) occurs. These interferences are controlled by the longitudinal momentum transfer $q_c = 1/t_c$ in the process of γ^* radiation by a projectile quark of energy E_q , $qN \rightarrow \gamma^* q X$,

$$q_c = \frac{M_{\gamma^*q}^2 - m_q^2}{2E_q}, \quad (3)$$

where we assume energy conservation, and the invariant mass squared of the γ^*q pair is

$$M_{\gamma^*q}^2 = \frac{M^2}{\alpha} + \frac{m_q^2}{1-\alpha} + \frac{q_T^2}{\alpha(1-\alpha)}. \quad (4)$$

One arrives at a similar estimate with help of the uncertainty principle. Indeed, a quark can violate energy conservation by fluctuating into γ^*q for a time $\Delta t \sim 1/(M_{\gamma^*q} - m_q)$ in the quark's rest frame. Applying the Lorentz gamma-factor $\gamma \sim 2E_q/(M_{\gamma^*q} + m_q)$ one reproduces the lifetime $t_c = 1/q_c$ in the lab frame as given by (3).

The intuitive space-time pattern related to the coherence time for DY pair production off nuclei is rather obvious. In the limit of short coherence time (relevant for the SPS energy) the initial state interactions are predominantly soft, since the hard fluctuation containing the heavy dilepton appears only deep inside the nucleus and is immediately freed on mass shell via the interaction with a bound nucleon.

On the other hand, if the coherence length substantially exceeds the size of the nucleus (as expected for the energies of RHIC for x_F greater than about 0.5 and the LHC for essentially all x_F), the hard fluctuation is created long in advance of the interaction with the nucleus, which acts as a whole in freeing the fluctuation. Since different target nucleons compete with each other, the DY cross section is subject to shadowing.

In this paper, we study nuclear effects in the limit of long coherence time. This is a most interesting regime, where interference effects are maximal and all the nucleons having the same impact parameter participate coherently in the DY process. A special advantage of the color-dipole approach is that it allows one to incorporate nuclear shadowing via a simple eikonalization of the dipole cross section $\sigma_{q\bar{q}}^N$ [16, 9] (see next section). This follows from the fact that in this limit the dipole size is “frozen” by Lorentz time dilation.

A projectile quark can develop more complicated fluctuations that involve gluons in addition to the heavy photon. These correspond to Fock states $|q\gamma^*G\rangle$, $|q\gamma^*2G\rangle$, etc. Interaction of these fluctuations with the nucleus is also affected by shadowing, which may be even stronger than for $|q\gamma^*\rangle$ provided that the fluctuation lifetime is long compared with nuclear size. This additional shadowing is, in the parton model, related to the shadowing of gluons resulting from gluon fusion at small x_2 (see Sect. 3).

One might think that in the case of pA collisions shadowing for DY can be easily predicted relying on QCD factorization and using data for shadowing in DIS off nuclei. However, data at small x are available only at very low Q^2 , where neither factorization nor DGLAP evolution are expected to be valid. Additionally, one should be cautious applying factorization at large x_1 where, as we pointed out above, higher twist corrections are rather large [3]. In particular, the Bjorken x of the target, x_2 , reaches its minimal value as $x_1 \rightarrow 1$; therefore, factorization predicts the maximal strength for shadowing. However, shadowing for the DY process vanishes in this limit. Indeed, since $\alpha > x_1$, the invariant mass Eq.(4) increases (for massive quarks and/or nonzero q_T), leading to the disappearance of the coherence length.

We do not make a fit to the observed shadowing in DIS on nuclei. We rather follow the logic of the conventional Glauber approach, where one is permitted to make fits to the data for nucleon-nucleon collisions but then predict nuclear effects in a parameter-free way. Indeed, we use the phenomenological dipole cross section on a nucleon target [17] fitted to the data for ep DIS from HERA that cover a range of energies much higher than that available from fixed-target nuclear shadowing data. The DY cross section calculated with this phenomenological cross section is supposed to include all higher-order corrections and higher twist effects.

Another important advantage of our approach is the possibility of calculating nuclear effects in the transverse momentum distribution of DY pairs. This is a difficult problem within the parton model. The phenomenon of nuclear broadening of the dilepton transverse momentum looks very different at low (short t_c) and high (long t_c) energies. If t_c is short, a hard fluctuation containing the heavy dilepton is created deep inside the nucleus just before the interaction that releases it. Meanwhile, the incident hadron may have soft initial state interactions in the nucleus. Although these do not generate DY dileptons, they do increase the mean transverse momentum of the fast partons of the projectile. Indeed, a fast parton experiencing multiple interactions performs something like Brownian motion in the plane of transverse momenta. As a result, the parton arrives at the point of the DY pair creation with increased transverse momentum. Information about the enhanced transverse momentum of the projectile quark in a nucleus compared to a proton target is carried away undisturbed by the dilepton pair. Nuclear broadening in the limit of short coherence time was investigated previously in [18].

At first glance, the observed broadening of the dilepton transverse momentum in the parton model might be viewed as arising from an increased transverse momentum of quarks and antiquarks in the nucleus. However, such a conclusion contradicts the usual picture of a nucleus boosted to the infinite momentum frame. There, nucleons and their parton clouds are well separated and do not overlap at large x_2 , just as in the nuclear rest frame. We know that only at very small x_2 do the parton clouds overlap and fuse leading to nuclear

shadowing. Such a fusion process results not only in suppressing the parton density, but it also increases the transverse momenta of the partons. Thus, shadowing and q_T broadening at small x_2 are closely related processes; no broadening is possible without shadowing. However, the regime of short t_c corresponds to large x_2 , where neither shadowing, nor q_T broadening is expected for the nuclear parton distribution function. Thus, we face a puzzle: nuclear broadening of the transverse momentum distribution of DY pairs calculated in the nuclear rest frame and observed experimentally has no analog within the parton model. This puzzle was resolved a long time ago by Bodwin, Brodsky and Lepage [19], who found that in the regime of short coherence length initial state interactions leading to q_T broadening violate QCD factorization and should not be translated into a modification of the nuclear quark distribution function. Likewise, initial state energy loss [2, 3] cannot be translated to a modification of x -distribution of partons in nuclei. This is a general statement which is applied to other hard reactions like high- q_T hadron production, etc.

In the regime of long coherence time $t_c \gg R_A$ relevant to RHIC and LHC, a very different mechanism is responsible for broadening of the transverse momentum distribution [12]. A high-energy projectile quark emits a dilepton fluctuation (via a virtual time-like photon) long before its interaction with the nucleus. These components of the fluctuation, the recoil quark and the dilepton, do not “talk” to each other because of Lorentz time dilation. Therefore, multiple interactions of the quark in nuclear matter seem to have no further influence on the produced dilepton and no broadening of the transverse momentum is expected. However, this conclusion is not correct. While it is true that different ingredients of the fluctuation cannot communicate, not all fluctuations contribute to DY pair production in the same way: The harder the fluctuation, that is the larger the intrinsic relative transverse momentum between the quark and dilepton, the stronger the kick from the target required for loss of coherence, i.e. for the fluctuation to be produced on mass shell. Large γ^*q -fluctuations (which have a low intrinsic transverse momentum) have a high probability to lose coherence in the first scattering on the surface of the nucleus. Therefore, the contribution to the DY cross section from these configurations scales as $A^{2/3}$, resulting in a nuclear suppression of the DY cross section at low q_T . Due to multiple interaction of the projectile quark a nucleus provides a larger transverse momentum than a nucleon target and hence is able to break up smaller fluctuations than a nucleon. This enhances the DY cross section at intermediate q_T . At high q_T multiple scatterings are not important any more, just a single high q_T scattering dominates, eliminating the nuclear enhancement. This is a result of the power q_T dependence of the cross section predicted by QCD. Since small q_T dileptons are suppressed while large q_T dileptons are not, the mean transverse momentum of DY pairs is increased. Thus, at long t_c , the mechanism behind nuclear broadening is color filtering [20].

This paper is organized as follows. We explain the main ideas of the light-cone approach in the introduction. The key ingredient of this method, the universal color dipole cross section for a $q\bar{q}$ pair interacting with a nucleon, is known from phenomenology. In Sect. 2, we explain how nuclear effects are treated in the color dipole approach. In particular, we describe, how nuclear gluon shadowing has to be included along with the $q\bar{q}$ -nucleus cross section. The results for gluon shadowing are presented in Sect. 3. The results of our calculations for the DY cross section in $p(D) + A$ collisions, and predictions for RHIC and LHC, can be

found in Sect. 4. Nuclear modification of the DY pair transverse momentum is calculated for the energies of RHIC and LHC in Sect. 5. We find that the so called Cronin effect, nuclear enhancement of the DY cross section at medium-large q_T , is nearly compensated at RHIC energies but is expected to have a large magnitude at LHC. We conclude that nuclear broadening of the DY transverse momentum squared diverges logarithmically for transversely polarized photons if nuclear shadowing occurs. Differences in nuclear effects for radiation of longitudinally and transversely polarized photons lead to a specific nuclear modification of the DY polarization. Corresponding predictions are presented in Sect. 6. In addition, we find substantial deviation from the so called Lam-Tung relation [21]. Indeed, this relation is not supported by data, which is difficult to explain within the standard parton approach. In Sect. 7 we address the more difficult problem of nuclear effects in heavy ion collisions. We follow conventional wisdom and simplify the problem by employing QCD factorization. Nuclear shadowing for both sea and valence quarks is calculated within the LC dipole approach. In contrast to usual expectations, shadowing for valence quarks turns out to be larger than for the sea. We summarize the results and observations of this paper and present an outlook for further development and application of the LC dipole approach in Sect. 8.

2 The $q\bar{q}$ -nucleus cross section

In order to calculate the DY cross section in pA scattering, one has to replace $\sigma_{q\bar{q}}^N$ in Eq. (1) by the color dipole cross section on a nucleus, $\sigma_{q\bar{q}}^A(\rho, x)$, which is easy to calculate within the color dipole approach.

In the limit of long coherence time, the projectile quark may be decomposed into a series of Fock-states with frozen transverse separations. Since partonic configurations with fixed transverse separations in impact parameter space are interaction eigenstates [16], $\sigma_{q\bar{q}}^A(\rho, x)$ may be calculated using Glauber theory [22], i.e. via simple eikonalization of the $q\bar{q}$ -nucleon cross section,

$$\tilde{\sigma}_{q\bar{q}}^A(\rho, x) = 2 \int d^2b \left[1 - \left(1 - \frac{1}{2A} \sigma_{q\bar{q}}^N(\rho, x) T_A(b) \right)^A \right], \quad (5)$$

where b is the impact parameter, A is the nuclear mass number and

$$T_A(b) = \int_{-\infty}^{\infty} dz \rho_A(b, z) \quad (6)$$

is the nuclear thickness, i.e. the integral over the nuclear density. The possibility of eikonalization of a color dipole propagating through a nucleus suggested in [16] has been more rigorously justified recently in [18, 23, 24, 25]. We mark $\sigma_{q\bar{q}}^A$ in Eq. (5) with a tilde to indicate that it misses important contributions from higher Fock components, which motivates us to introduce an improved eikonal formula, Eq. (13), below. Note that at larger $x_2 \gtrsim 0.01$, when the coherence length becomes shorter than the nuclear radius, the eikonal approximation breaks down and one has to employ the Green function technique developed in [12].

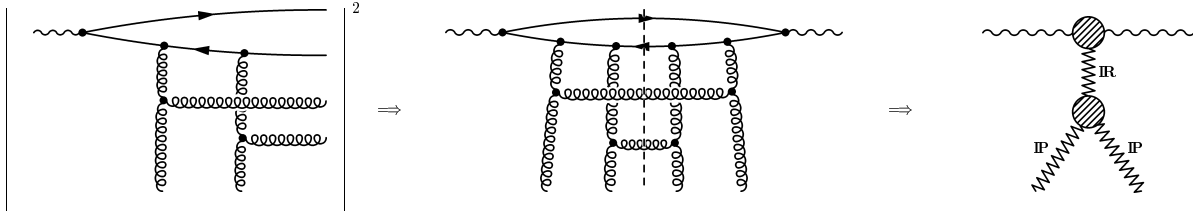


Figure 2: *The eikonal formula (5) takes only multiple rescatterings of the $|q\bar{q}\rangle$ -Fock component into account. This figure illustrates the amplitude for double scattering (left). When the amplitude is squared (middle), the gluon rungs combine into gluon ladders (Pomerons), which are enclosed into each other. In Regge theory, this contribution to the cross section is expressed in terms of the Pomeron-Pomeron-Reggeon vertex (right).*

The single-scattering term can be obtained by expanding (5) to first order in $\sigma_{q\bar{q}}^N(\rho, x)$. The dipole interacts with the target by exchange of a gluonic colorless system, the so called Pomeron. The unitarity cut of such an amplitude reveals multiple gluon radiation that is related to higher Fock states within the LC approach in the target rest frame. Thus, for single scattering, $\sigma_{q\bar{q}}^N$ takes all Fock states of the projectile parton into account, not only $|q\bar{q}\rangle$. The energy dependence of the dipole cross section is generated by the phase space of gluons from higher Fock states $|q\bar{q}G\rangle$, $|q\bar{q}GG\rangle$, \dots . Indeed, in the Born approximation, i.e. two gluon exchange, $\sigma_{q\bar{q}}^N$ would be independent of x .

Calculation of $\sigma_{q\bar{q}}^N$ from first principles is still a challenge. We rely on phenomenology and employ the parameterization of Golec-Biernat and Wüsthoff [17] motivated by the saturation model,

$$\sigma_{q\bar{q}}^N(\rho, x) = \sigma_0 \left[1 - \exp\left(-\frac{\rho^2 Q_0^2}{4(x/x_0)^\lambda}\right) \right], \quad (7)$$

where $Q_0 = 1$ GeV and the three fitted parameters are $\sigma_0 = 23.03$ mb, $x_0 = 0.0003$, and $\lambda = 0.288$. This dipole cross section vanishes $\propto \rho^2$ at small distances, as implied by color transparency, and levels off exponentially at large separations. The authors of [17] are able to fit all available HERA data with a quite low χ^2 and can also describe diffractive HERA data.

We now turn to the multiple scattering terms. Describing shadowing for DY is simplified if we make use of the fact that the dipole cross section entering the formula for dilepton production, Eq. (1), is the same as that needed to calculate the DIS cross section. We may thus illustrate the physics of Eq. (5) in fig. 2, where the double-scattering term for a $q\bar{q}$ -dipole is depicted. In terms of Regge phenomenology, the double scattering of the $q\bar{q}$ -pair corresponds to the Pomeron-Pomeron-Reggeon vertex. Note that (5) accounts for not only the double-scattering term, but also for all higher-order rescatterings of the $q\bar{q}$ -pair. The n -fold scattering graph has n gluon ladders, which are enclosed into each other.

Rescatterings of higher Fock states, containing gluons are omitted in (5). This equation corresponds to gluon radiation in the Bethe-Heitler regime, where each interaction of the

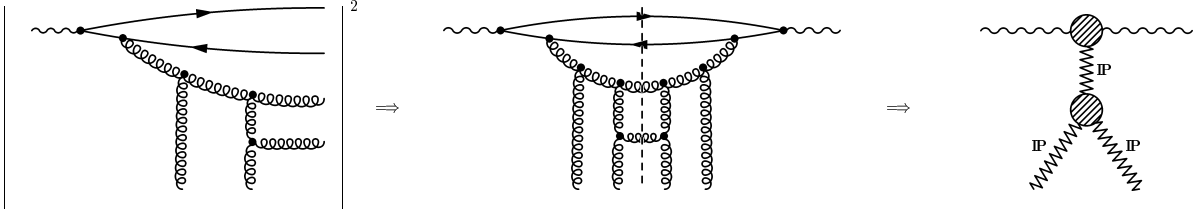


Figure 3: *At high energy, the lifetime of higher Fock states becomes long enough for multiple scattering. Shown here is the double-scattering amplitude for the $|q\bar{q}G\rangle$ -Fock state. In Regge theory, this process is expressed in terms of the triple-Pomeron vertex (right). The eikonal formula (5) is improved by multiplying $\sigma_{q\bar{q}}$ by the gluon shadowing ratio R_G , Eq. (13), to include these contributions also.*

quarks leads to independent radiation of the entire spectrum of gluons. However, interferences known as the Landau-Pomeranchuk effect, lead to a suppression of gluon radiation. This shadowing correction is taken into account via multiple interactions of radiated gluons in the nucleus [26] and leads to an additional suppression of the DY cross section. At low x the lifetime of these higher Fock states becomes significantly longer than the mean inter-nucleon distance, and they can scatter more than once inside the nucleus, as illustrated in fig. 3. In this case, which occurs at RHIC and LHC energies, (5) needs to be modified to include also these rescattering.

In order to include processes like the one illustrated in fig. 3, it is useful to note that the rescattered gluon can be interpreted as the first rung of a single gluon ladder exchanged between the $q\bar{q}$ -pair and the target. In Regge phenomenology, rescattering of gluons leads to the triple-Pomeron vertex fig. 3(right), which can be regarded as a correction to the single-scattering term. More precisely, it leads to a reduction of the nuclear gluon density G_A because the two Pomerons from the target in fig. 3(right) fuse into a single one before interacting with the pair. Indeed, multiple scatterings of higher Fock states containing gluons are known as the effect of gluon shadowing [26] and lead to an additional suppression of the DY cross section. In the infinite momentum frame of the nucleus, gluon clouds of different nucleons overlap and fuse at small x [27, 5], fig. 3(right), thereby reducing the gluon density at small x . Although the corrections for gluon rescatterings the nuclear rest frame and gluon fusion (in the nuclear infinite momentum frame) look very different, this is the same phenomenon seen from different reference frames. Of course, observables are Lorentz invariant, and both effects lead to a reduction of the DY cross section.

Thus, the Pomeron-Pomeron fusion process in fig. 3(right) can be taken into account by multiplying $\sigma_{q\bar{q}}^N(\rho, x)$ by the gluon shadowing ratio

$$R_G(x, \tilde{Q}^2) = \frac{G_A(x, \tilde{Q}^2)}{AG_N(x, \tilde{Q}^2)} \equiv 1 - \Delta R_G(x, \tilde{Q}^2), \quad (8)$$

as calculated in Appendix A. The single-scattering term then reads

$$\begin{aligned}\sigma_{q\bar{q}}^A(x, \rho) &= \sigma_{q\bar{q}}^N(\rho, x) \int d^2b R_G(x, \tilde{Q}^2, b) T_A(b) + \dots, \\ &= A \sigma_{q\bar{q}}^N(\rho, x) \left[1 - \frac{1}{A} \int d^2b \Delta R_G(x, \tilde{Q}^2, b) T_A(b) \right] + \dots,\end{aligned}\quad (9)$$

where gluon shadowing as a function of impact parameter b is given in Eqs. (A.20) and (A.21).

The first term in the brackets of (9) stands for the direct exchange of a Pomeron, while the second (negative) term represents the correction due to the Pomeron fusion process depicted in fig. 3. This recipe becomes even more clear from the relation, valid at $\rho \rightarrow 0$, [28],

$$\sigma_{q\bar{q}}^N(\rho, x) \Big|_{\rho \rightarrow 0} = \frac{\pi^2}{3} \alpha_s \left(\frac{\lambda}{\rho^2} \right) \rho^2 G_N \left(x, \frac{\lambda}{\rho^2} \right). \quad (10)$$

In (9), the gluon density of the proton in (10) was replaced by the average gluon density of the nucleus,

$$\sigma_{q\bar{q}}^N(\rho, x) \Big|_{\rho \rightarrow 0} \Rightarrow \frac{\pi^2}{3} \alpha_s \left(\frac{\lambda}{\rho^2} \right) \rho^2 \frac{1}{A} G_A \left(x, \frac{\lambda}{\rho^2} \right). \quad (11)$$

It is clear from (9) that the effective dipole cross section on a bound nucleon appears to be reduced due to gluon shadowing. We also see from (10) that R_G has to be evaluated at a scale $\tilde{Q}^2 = \lambda/\rho^2$.

The specific fusion processes that are included in (9) depends on the approximation in which gluon shadowing R_G is evaluated. For our actual calculations (see Sect. 3) nuclear shadowing for gluons is calculated within the Green function formalism for a $|q\bar{q}G\rangle$ fluctuation propagating through nuclear medium as developed in [29]. This means, that the single-scattering term in (9) is corrected not only for the $2\mathbf{IP} \rightarrow \mathbf{IP}$ Pomeron fusion term depicted in fig. 3(right), but also for all the $n\mathbf{IP} \rightarrow \mathbf{IP}$ fusion processes. Moreover, the Green function approach properly describes the finite lifetime of the $|q\bar{q}G\rangle$ -state. This is important, because even when the $q\bar{q}$ -fluctuation lives much longer than the nuclear radius, the lifetime of the $|q\bar{q}G\rangle$ -state will be shorter.

For the rescattering terms, we can account for higher Fock states in the same way as in (9), namely by the replacement [30, 31, 32]

$$\sigma_{q\bar{q}}^N(\rho, x) \Rightarrow \sigma_{q\bar{q}}^N(\rho, x) R_G(x, \tilde{Q}^2, b), \quad (12)$$

i.e. the improved formula Eq. (5) for the $q\bar{q}$ -nucleus section reads,

$$\sigma_{q\bar{q}}^A(\rho, x) = 2 \int d^2b \left[1 - \left(1 - \frac{1}{2A} \sigma_{q\bar{q}}^N(\rho, x) R_G(x, \lambda/\rho^2, b) T_A(b) \right)^A \right]. \quad (13)$$

This expression includes also the contribution of higher Fock states containing more than one gluon. The higher-order multiple interactions of the $|q\bar{q}G\rangle$ Fock state correspond, as

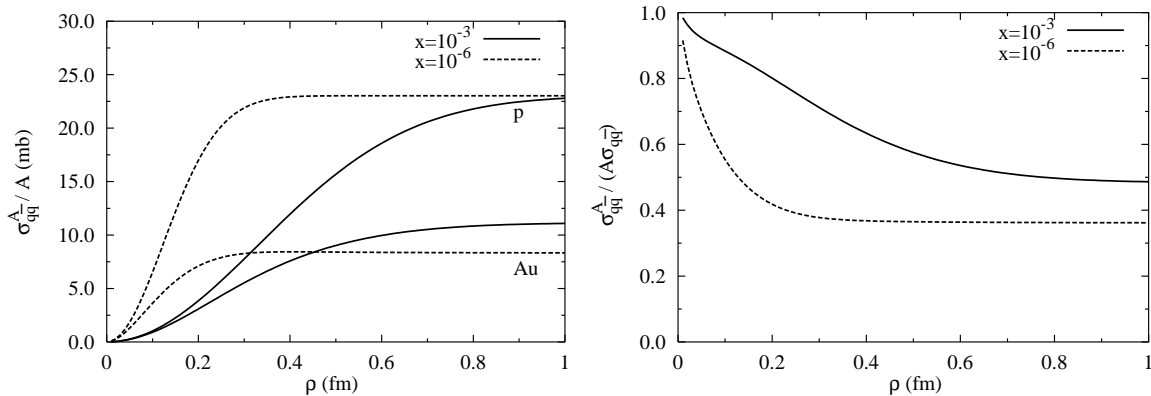


Figure 4: The figure on the left shows the $q\bar{q}$ -nucleus cross section (13) divided by the nuclear mass number A for two different values of x . The two lower curves (solid and dashed) are calculated for gold ($A = 197$) and the two upper curves for a proton. The figure on the right shows the $q\bar{q}$ -nucleus cross section divided by A times the dipole cross section (7). While large separations are strongly suppressed, small size dipoles are much less affected by the nucleus. Nuclear gluon shadowing is included in the calculation, as explained in the text. It slowly vanishes at small $q\bar{q}$ separations, which correspond to high \tilde{Q}^2 .

was mentioned, to multi-Pomeron fusion, $n\mathbf{IP} \rightarrow \mathbf{IP}$, while the Reggeon diagrams with $n\mathbf{IP} \rightarrow m\mathbf{IP}$ ($m \geq 2$) are missing. Those diagrams should be incorporated via the Fock components $|q\bar{q}mG\rangle$ containing two or more gluons. The modified expression Eq. (13) sums multiple interactions of the $q\bar{q}$ pair via $m\mathbf{IP}$ exchange (summed over m), each of which has the form of a fan $n\mathbf{IP} \rightarrow \mathbf{IP}$ (summed over n). We assume that each gluon in the Fock state $|q\bar{q}mG\rangle$ experiences multiple interactions independently of other gluons. This assumption corresponds to the Gribov's interpretation [33] of Glauber eikonal shadowing; namely, the unitarity cut of an n -fold scattering term must contain a simultaneous cut of all n Pomerons. It therefore corresponds to a nonplanar graph describing the independent multiple interactions of n projectile partons (see discussion in [31]).

Note that the GLR equation [5] can be obtained from Eq. (13) by expanding the r.h.s. up to quadratic order in $\sigma_{q\bar{q}}^N$. Though the higher order terms in this expansion may not be found in the large N_c , leading $\log(1/x)$ limit of QCD [34], their numerical influence on the DY cross section will be small because of the large dilepton mass.

We can now proceed to calculate $\sigma_{q\bar{q}}^A(x, \rho)$ according to (13). We briefly summarize our calculation of gluon shadowing (R_G) [29] in section 3. The results for the nuclear dipole cross section $\sigma_{q\bar{q}}^A(\rho, x)$ are depicted in fig. 4. Since (13) is a high-energy approximation, valid when the lifetime of the $q\bar{q}$ -pair exceeds the nuclear radius, these results are relevant at RHIC and LHC energies. At lower energies however, one has to take transitions between different eigenstates into account [12].

The plot on the l.h.s. of fig. 4 shows the dipole cross section itself. First, we discuss the

$q\bar{q}$ -proton cross section. The two upper curves show this quantity for two different values of x typical for RHIC and LHC. After a quadratic rise, $\sigma_{q\bar{q}}^N$ levels off and assumes an energy-independent saturation value of 23.03 mb. The onset of saturation, i.e. the flattening of the dipole cross section as function of ρ , is controlled by the saturation radius,

$$R_s^2(x) = \frac{2}{Q_0^2} \left(\frac{x_0}{x} \right)^\lambda, \quad (14)$$

which decreases with energy. The energy dependence of (7) correlates with ρ . At $\rho \ll R_s$, the dipole cross section grows with energy with the hard Pomeron intercept $\lambda = 0.288$, while at large separations, $\rho \gg R_s$, (7) becomes independent of energy. For more discussion on (7), refer to the original work [17].

We now turn our attention to the $q\bar{q}$ nucleus cross section $\sigma_{q\bar{q}}^A(\rho, x)$, Eq. (13), which is shown by the two lower curves in fig. 4 (left). In all calculations, we employ realistic parameterizations of nuclear densities from [35]. In addition to the expected suppression due to nuclear shadowing, one also sees that the saturation value of $\sigma_{q\bar{q}}^A$, which is almost at its geometrical limit $2\pi R_A^2$, is energy dependent. Moreover, $\sigma_{q\bar{q}}^A(\rho \rightarrow \infty, x)$ is a decreasing function of energy. This is a consequence of the gluon shadowing in (13). At very small x , gluon shadowing becomes strong, (see fig. 6) and the $q\bar{q}$ nucleus cross section lies below its geometrical limit. The stronger the gluon shadowing, the smaller the saturation value of $\sigma_{q\bar{q}}^A$. However, $R_G \rightarrow 1$ at $\rho \rightarrow 0$ since $\tilde{Q}^2 \sim 1/\rho^2 \rightarrow \infty$ (see fig. 6).

The nuclear suppression of the dipole cross section is plotted on the right-hand side of fig. 4. Small sizes are less affected by the nucleus than large sizes. This illustrates the effect of color filtering [20], which is the mechanism behind nuclear broadening of transverse momenta (see section 5). While small $q\bar{q}$ -pairs, which have large intrinsic transverse momenta according to the uncertainty principle, propagate through the nucleus almost undisturbed, large pairs (small transverse momenta) are absorbed, i.e. the coherence of the fluctuation is disturbed and the γ^* is freed. This effect leads to an increase of the mean transverse momentum.

3 Gluon shadowing in nuclei

The nuclear shadowing for gluons needed as input for the $q\bar{q}$ -nucleus cross section in (13) is calculated in the LC Green function approach developed in [29], where gluon shadowing is calculated from shadowing of the $|q\bar{q}G\rangle$ Fock component of a longitudinally polarized photon. In this section, we briefly review the approach of [29] and present the results of our calculation for gluon shadowing as function of x , Q^2 and the length L of the path in the nuclear medium.

Longitudinal photons can serve to measure the gluon density because they effectively couple to color-octet-octet dipoles. This can be understood in the following way: the light-cone wave function for the transition $\gamma_L^* \rightarrow q\bar{q}$ does not allow for large, aligned jet configurations. Thus, unlike the transverse case, all $q\bar{q}$ dipoles from longitudinal photons have size $1/Q^2$ and the double-scattering term vanishes like $\propto 1/Q^4$. The leading-twist contribution for the

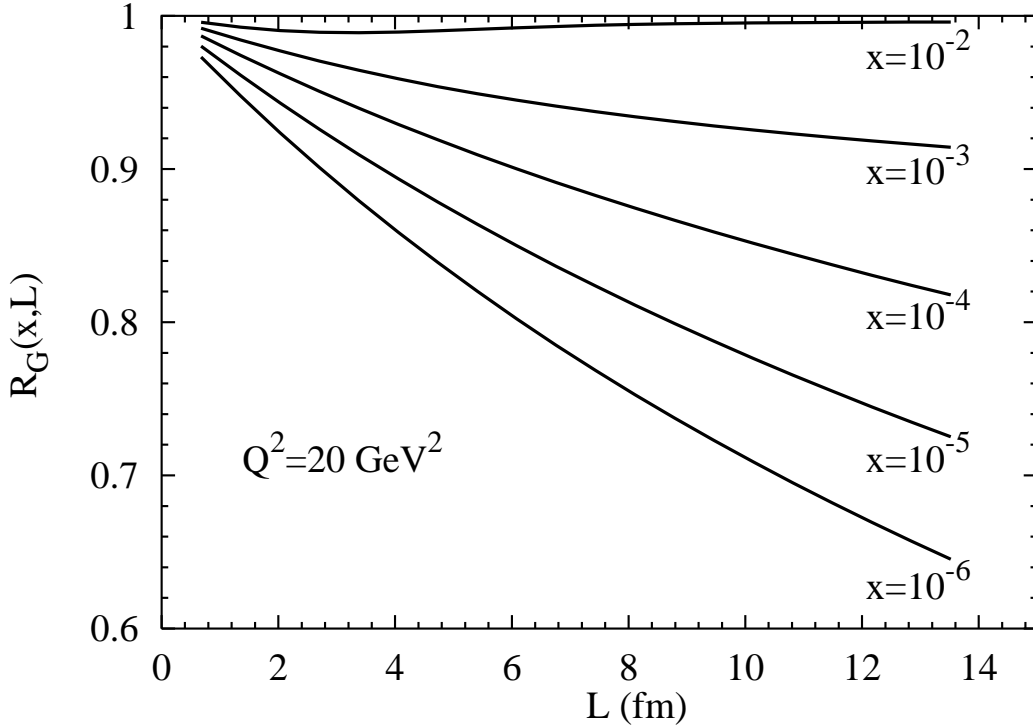


Figure 5: *Gluon shadowing vs. the length of the nuclear medium $L = 2\sqrt{R_A^2 - b^2}$, where b is the impact parameter and R_A the nuclear radius. All curves are for $Q^2 = 20 \text{ GeV}^2$ but for different values of x .*

shadowing of longitudinal photons arises from the $|q\bar{q}G\rangle$ Fock state of the photon. Here again, the distance between the q and the \bar{q} is of order $1/Q^2$, but the gluon can propagate relatively far from the $q\bar{q}$ -pair. In addition, after radiation of the gluon, the pair is in an octet state. Therefore, the entire $|q\bar{q}G\rangle$ -system appears as a GG -dipole, and the shadowing correction to the longitudinal cross section is just the gluon shadowing we want to calculate.

A critical issue for determining the magnitude of gluon shadowing is the distance the gluon can propagate from the $q\bar{q}$ -pair in impact parameter space, i.e. knowing how large the GG dipole can become. This value could be extracted from single diffraction data in hadronic collisions in [29] because these data allow the diffractive gluon radiation (the triple-Pomeron contribution in Regge phenomenology) to be unambiguously singled out. The diffraction cross section ($\propto \rho^4$) is even more sensitive to the dipole size than the total cross section ($\propto \rho^2$) and is therefore a sensitive probe of the mean transverse separation. It was found in [29] that the mean dipole size must be of the order of $r_0 = 0.3 \text{ fm}$, considerably smaller than a light hadron. A rather small gluon cloud of this size surrounding the valence quarks is the only way that is known to resolve the long-standing problem of the small size of the triple-Pomeron coupling. The smallness of the GG dipole is incorporated into the LC approach by a nonperturbative interaction between the gluons.

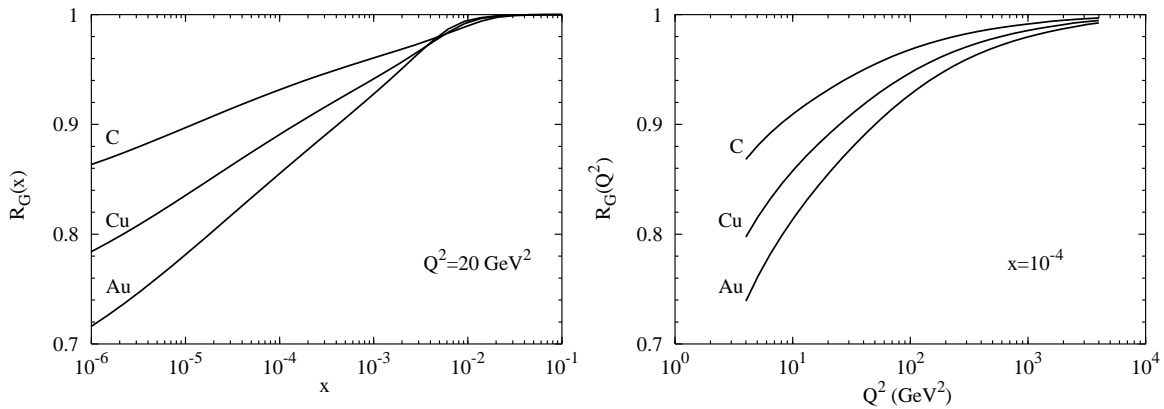


Figure 6: *The x - and Q^2 -dependence of gluon shadowing for carbon, copper and gold. The x -dependence is shown for $Q^2 = 20 \text{ GeV}^2$, while the figure on the right is calculated for $x = 10^{-4}$.*

Note that the small value of r_0 dictated by data for diffraction is consistent with the results of other approaches. Indeed, the same small size characterizing gluonic fluctuations was found in the instanton liquid model [36], in the QCD sum rule analysis of the gluonic formfactor of the proton [37], and it also follows from lattice calculations [38]. Note that the value of r_0 also limits the Q^2 -range where the approximation $q\bar{q}G \approx GG$ is valid. One has to ensure that $Q^2 \gg 1/r_0^2$, otherwise the $q\bar{q}$ pair is not pointlike compared to the size of the entire Fock state.

Our results for gluon shadowing as a function of the length of the nuclear medium at impact parameter b are shown in fig. 5. The calculations are performed for lead with a uniform nuclear density of $\rho_A = 0.16 \text{ fm}^{-3}$. Details are presented in Appendix A. The small size of the GG dipole leads to a rather weak gluon shadowing (except for specific reactions where the $q\bar{q}$ pair is colorless [31]). For most values of x , gluon shadowing increases as a function of L as one would expect. At the largest value of $x = 0.01$, however, gluon shadowing becomes smaller as L increases, and R_G approaches 1. Although this behavior seems to be counterintuitive, it can be easily understood by noting that at $x = 0.01$ the coherence length of the $|q\bar{q}G\rangle$ -Fock state becomes very small and the formfactor of the nucleus suppresses shadowing [39]. The curves shown in fig. 5 are the ones which actually enter our calculation for DY via the $q\bar{q}$ -nucleus cross section (13). The values of x entering our calculation are $x \approx 10^{-3}$ for RHIC and $x \approx 10^{-6}$ for LHC.

We also calculate gluon shadowing as function of x at fixed Q^2 and as a function of Q^2 at fixed x , integrated over the impact parameter b . The results are shown in fig. 6. In the left-hand plot, one observes that gluon shadowing vanishes for $x > 0.01$. This happens because the lifetime of the $|q\bar{q}G\rangle$ -fluctuation becomes smaller than the mean internucleon distance of $\sim 2 \text{ fm}$ as x exceeds 0.01. Indeed, in [39] an average coherence length of slightly less than 2 fm was found for the $|q\bar{q}G\rangle$ -state at $x = 0.01$ and large $Q^2 \gg 1/r_0^2$. Note that gluon shadowing sets in at a smaller value of x than quark shadowing because the mass of a $|q\bar{q}G\rangle$ -state is larger than the mass of a $|q\bar{q}\rangle$ -state. This delayed onset of gluon shadowing

was already found in [29]. We also point out that gluon shadowing is even weaker than quark shadowing in the x -range plotted, because the small size of the GG -dipole overcompensates the Casimir factor in the GG -proton cross section, $\sigma_{GG}^N = (9/4)\sigma_{q\bar{q}}^N$. The plot on the right-hand side of fig. 6 shows the Q^2 -dependence of gluon shadowing and clearly demonstrates that gluon shadowing is a leading-twist effect, with R_G only very slowly (logarithmically) approaching unity as $Q^2 \rightarrow \infty$.

4 Nuclear shadowing for DY pair production in pA - and DA -collisions

Nuclear shadowing for the DY process was first observed in proton-nucleus (pA) collisions at large x_F [1] in the E772 experiment. The shadowing effect will also be present in the energy range of RHIC and LHC. Since RHIC will probably first measure the DY cross section from deuterium-nucleus (DA) rather than pA collisions, we perform calculations for both, pA and DA collisions.

The dipole formulation provides the following explanation of shadowing in the DY process. When the coherence time is long, one of the projectile quarks develops a γ^*q -fluctuation long before it reaches the target. If the transverse momentum transfer from the target is large enough to resolve the fluctuation, the virtual photon is freed and eventually is observed as a lepton pair in the detector. In the case of a nuclear target, the set of struck nucleons compete to free the virtual photon. If the $|\gamma^*q\rangle$ -state has a very small transverse size, it can propagate through the entire nucleus because none of the bound nucleons can provide a kick strong enough to resolve the $|\gamma^*q\rangle$ structure in the incident quark. These small fluctuations have the same small probability to interact with any nucleon, so they will not be shadowed. On the other hand, if the fluctuation is sufficiently large in size, only a small momentum transfer is necessary to resolve the photon. Thus, the coherence of a large fluctuation will be destroyed with high probability already in the first collision on the surface of the nucleus. Nucleons deeper in the nucleus do not add much to the probability of freeing the γ^* . Thus, this probability nearly saturates for these extremely large fluctuations, and the DY cross section will scale like $A^{2/3}$. From these considerations, we can find two necessary conditions for shadowing [39],

- The γ^*q fluctuation must have a lifetime long enough to allow for at least two scatterings during the coherence time t_c .
- The γ^*q fluctuation must have a large freeing cross section³, i.e. its transverse size must be sufficiently large.

³One should distinguish between the freeing and the total cross sections of a fluctuation. The latter is always large for a colored quark and all its fluctuations, while the former is driven by the difference between scattering amplitudes of different fluctuations ($|q\rangle$ and $|q\gamma^*\rangle$ in our case). Since it is only the quark that interacts in each of these Fock states, the freeing cross section is controlled by the relative transverse displacement of the quarks within different fluctuations. This is how the dipole cross section comes about.

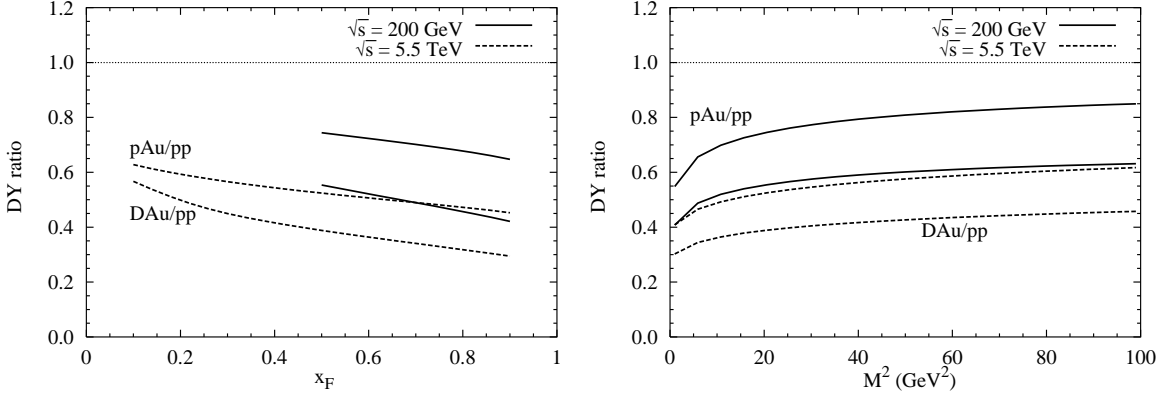


Figure 7: *Shadowing for the total DY cross section in proton – gold (upper curves) and deuterium – gold (lower curves) collisions at the energies of RHIC and LHC as function of Feynman x_F and dilepton mass M^2 , respectively. The left-hand figure is calculated for $M = 4.5$ GeV. The figure on the right for $x_F = 0.5$.*

The first condition is assumed to be fulfilled throughout this paper, where we consider only the case of infinite t_c . The dependence of shadowing on the fluctuation size is encoded in the $q\bar{q}$ -nucleus cross section (13).

Note that since the γ^*q -fluctuation is formed long before it reaches the target, the dilepton is unaffected by quark energy loss. Thus, the entire suppression of the DY cross section at very low x_2 , say $x_2 < 0.001$, is due to shadowing, and we do not need to worry about energy loss. This is different at the lower fixed-target energies [1], where the observed depletion of the DY cross section originates from a combination of shadowing and energy loss [2, 3]. The complimentary behavior of shadowing and energy loss is discussed in more detail in [3]: long t_c means that only shadowing occurs, while for short t_c , one observes only energy loss.

To obtain the cross section for an incident hadron, the partonic cross section (1) has to be weighted with the quark (and antiquark) distributions, $q(x)$, of the projectile hadron, and one has to include in addition the factors necessary to account for the decay of the virtual photon into the dilepton. For an incident proton, this cross section becomes

$$\frac{d^4\sigma(pA \rightarrow l\bar{l}X)}{dM^2 dx_F} = \frac{\alpha_{em}}{3\pi M^2} \frac{x_1}{x_1 + x_2} \int_{x_1}^1 \frac{d\alpha}{\alpha^2} \sum_f Z_f^2 \left\{ q_f\left(\frac{x_1}{\alpha}, M^2\right) + q_{\bar{f}}\left(\frac{x_1}{\alpha}, M^2\right) \right\} \quad (15)$$

$$\times \frac{d\sigma(qA \rightarrow \gamma^*X)}{d \ln \alpha},$$

where Z_f is the charge of a quark of flavor f . We assume that the the same expression (15) applies for both proton and deuteron projectiles, so that the only difference between these cases is that the flavor sum ranges over the quarks of the proton *and* neutron in the case of an incident deuteron. Nuclear effects in the deuterium structure function and finite-size effects are neglected, and isospin symmetry is assumed.

For a calculation that can actually be compared to data, we employ the CTEQ5L parameterization [40] (taken from CERNLIB [41]) for $q_{f,\bar{f}}$. Note that the projectile quark distributions enter at large $x = x_1/\alpha > x_1$, where they are well known. Thus, the uncertainty arising from the choice of parton distributions is minimal. However, these parton distributions are different for the proton and deuterium, so that the pA and DA DY cross section are not trivially related. Shadowing can now be obtained by evaluating (15) and (1), with $\sigma_{q\bar{q}}^A(\rho, x_2)$ taken from (13), and dividing by A times the analogous calculation with the $q\bar{q}$ -proton cross section (7). In the case of the deuterium projectile, we divide by $2A$. The nuclear density parameterizations are taken from [35].

The result as function of x_F and dilepton mass M at different energies is shown in fig. 7. For each energy (RHIC and LHC) we calculated pAu and DAu collisions and normalized both to pp collisions. Note that the DAu curve is always below the pAu curve (for a given energy). This is because of the different flavor structure of deuterium and the fact that d -quarks are weighted with a factor $Z_d^2 = 1/9$ in (15), compared to the factor $Z_u^2 = 4/9$ for u -quarks. For the RHIC energy of $\sqrt{s} = 200$ GeV, we calculate only for $x_F > 0.5$ to make sure that the fluctuation lifetime significantly exceeds the nuclear radius. At the very high LHC energy of $\sqrt{s} = 5.5$ TeV, the coherence time is much larger than the nuclear radius for any value of x_F (except at the very endpoints). Thus, the entire x_F -range is shadowed. Shadowing is especially strong at LHC energies at large x_F , where x_2 can become as small as $x_2 \approx 10^{-6}$. At such low x_2 , the effects of gluon shadowing leads to a sizable additional suppression of the DY cross section. Without the gluon shadowing contribution in (13), shadowing of the DY reaction at LHC would be strongly underestimated. The mass dependence of shadowing in DY is shown in the plot on the right-hand side of fig. 7. The weak dependence on M reflects the fact that shadowing for DY is a leading-twist effect, just as for DIS. Indeed, configurations with $\alpha \rightarrow 1$ in (1) and (15) are the analog of Bjorken's aligned jet configurations in DIS [11], which make shadowing persist as $M \rightarrow \infty$.

We also investigate the A - and the impact parameter dependence of shadowing, with the results shown in fig. 8. The amount of shadowing, *i.e.* the difference from unity in fig. 8, is to a good approximation proportional to $A^{1/3}$. The deuterium curves in fig. 8 do not of course go to unity at $A = 1$ or $b \rightarrow \infty$; the flavor suppression remains in these limiting cases. We point out that it is a special advantage of the dipole approach that it naturally predicts the impact parameter dependence of nuclear effects. To obtain the b dependence, one simply eliminates the b integral in (13) and divides by the nuclear thickness $T(b)$ instead of A .

5 Nuclear modification of the DY transverse momentum distribution in pA - and DA -collisions

The differential DY cross section as a function of the dilepton transverse momentum q_T can be calculated in the dipole formulation as well. At the energies relevant for RHIC and LHC, the transverse momentum distribution of DY pairs from $p(D) + A$ collisions can be written

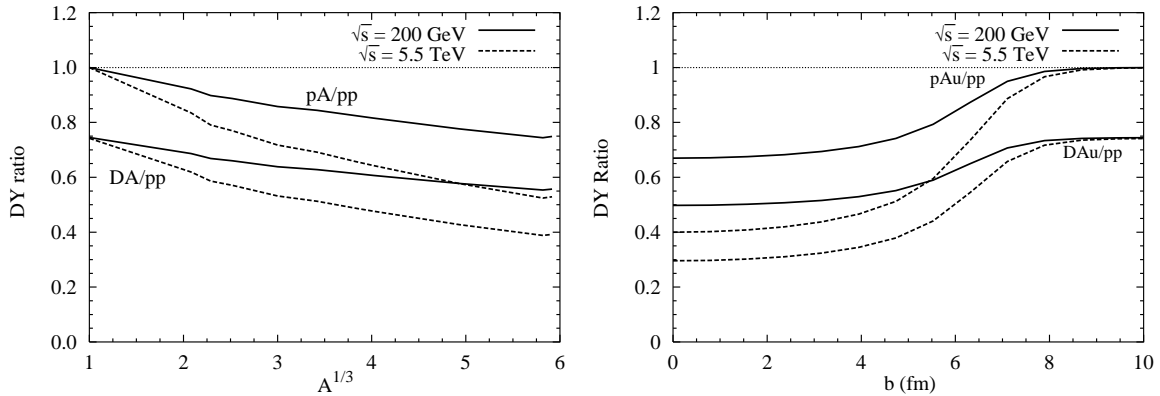


Figure 8: *Shadowing for the total DY cross section as a function of $A^{1/3}$ and impact parameter b . Both figures are calculated for $M = 4.5$ GeV and $x_F = 0.5$. In each plot, the lower pair of curves is for deuteron – gold scattering (DAu) and the two upper curves are for proton – gold collisions (pAu).*

in frozen approximation [12, 13],

$$\frac{d^4\sigma(pA \rightarrow l\bar{l}X)}{dM^2 dx_F d^2q_T} = \frac{\alpha_{em}}{3\pi M^2} \frac{x_1}{x_1 + x_2} \int_{x_1}^1 \frac{d\alpha}{\alpha^2} \sum_f Z_f^2 \left\{ q_f \left(\frac{x_1}{\alpha} \right) + q_{\bar{f}} \left(\frac{x_1}{\alpha} \right) \right\} \frac{d\sigma(qA \rightarrow \gamma^* X)}{d \ln \alpha d^2q_T}, \quad (16)$$

in analogy to Eq. (15). The differential cross section for heavy-photon radiation in a quark-nucleus collision was derived in [12],

$$\begin{aligned} \frac{d\sigma(qA \rightarrow \gamma^* X)}{d \ln \alpha d^2q_T} &= \frac{1}{(2\pi)^2} \int d^2\rho_1 d^2\rho_2 \exp[i\vec{q}_T \cdot (\vec{\rho}_1 - \vec{\rho}_2)] \Psi_{\gamma^*q}^*(\alpha, \vec{\rho}_1) \Psi_{\gamma^*q}(\alpha, \vec{\rho}_2) \\ &\times \frac{1}{2} \left[\sigma_{q\bar{q}}^A(\alpha\rho_1, x_2) + \sigma_{q\bar{q}}^A(\alpha\rho_2, x_2) - \sigma_{q\bar{q}}^A(\alpha|\vec{\rho}_1 - \vec{\rho}_2|, x_2) \right]. \end{aligned} \quad (17)$$

In this expression, the z -axis is parallel to the momentum of the projectile quark. Integrating Eq. (17) over q_T we arrive at the cross section Eq. (1). Three of the four integrations in (17) can be performed analytically for an arbitrary form of the dipole cross section $\sigma_{q\bar{q}}^N$ [42]. The details of calculations are moved to Appendix B. Since the remaining integration still has to be performed over an oscillating function, the q_T -range in which numerical calculations are feasible is limited. We calculate up to $q_T = 10$ GeV, which covers the experimentally interesting region.

As in the preceding section, we perform calculations for pA and for DA scattering. Our results for the differential DY cross section for transverse and longitudinal pairs are shown in fig. 9. We show curves only for pA in this figure, because the difference between pA and DA is hardly visible on the logarithmic scale. Even though x_2 increases as function of q_T , at $q_T = 10$ GeV the coherence time t_c is still larger than the nuclear radius. As already observed in [13], the differential cross section does not diverge at zero transverse momentum

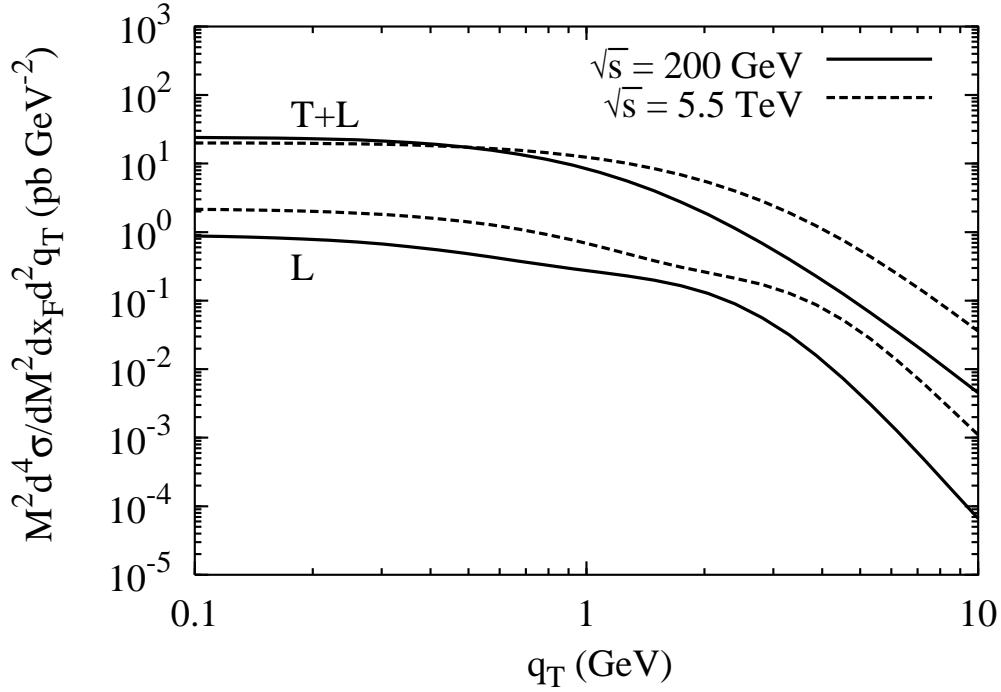


Figure 9: Absolute value of the differential DY cross section for pAu scattering, divided by $A(= 197)$. The curves are predictions for RHIC ($\sqrt{s} = 200$ GeV) and LHC ($\sqrt{s} = 5.5$ TeV) for the dilepton mass of $M = 4.5$ GeV and $x_F = 0.5$. The upper two curves show the sum of transverse and longitudinal cross section ($T + L$) and the lower two curves (L) separately show the longitudinal cross section.

because of the flattening of the dipole cross section at large separations. On the partonic level, we reproduce the same asymptotic behavior that is expected in the standard parton model,

$$\frac{d\sigma_T(qp \rightarrow \gamma^* X)}{d^2 q_T} \propto \frac{1}{q_T^4} \quad \text{for } q_T \rightarrow \infty \quad (18)$$

and

$$\frac{d\sigma_L(qp \rightarrow \gamma^* X)}{d^2 q_T} \propto \frac{1}{q_T^6} \quad \text{for } q_T \rightarrow \infty. \quad (19)$$

Embedding the partonic cross section (17) into the hadronic environment as in (16) will lead to a somewhat steeper decay at large q_T , reflecting the decrease of the structure function F_2 of the projectile with x_1 and the increase of x_1 with q_T . While this effect is quite strong at $x_F = 0$ and fixed target energies, it becomes negligible at large x_F and the high cm . energies at RHIC and LHC. Indeed, even at $q_T = 10$ GeV, the asymptotic limit is not yet fully reached. The q_T dependence is still slightly less steep than in (18).

To see the effect of nuclear shadowing and antishadowing we divide the nuclear differential

cross section by A times that of the nucleon ($2A$ for DA scattering). Then, nuclear effects manifest themselves as a deviation from unity. The results of calculations (see Appendix B) for gold at the energies of RHIC and LHC are presented in fig. 10 for the unpolarized (top) and longitudinally polarized (bottom) DY cross section ratios. Also, the difference between pA (left) and DA (right) now becomes clearly visible. As already explained in Sect. 4, this difference is due to the larger abundance of d -quarks in deuterium. Note that we neglected nuclear effects in deuterium and assumed isospin symmetry for the DA curves.

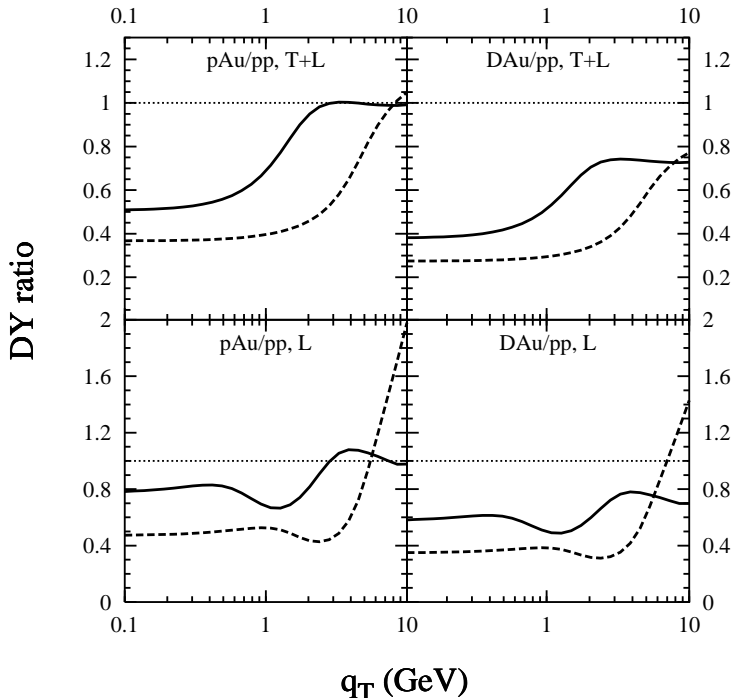


Figure 10: Nuclear effects on the DY transverse momentum distribution. Curves show the DY cross sections for pAu (left) and deuterium – gold (right) collisions per nucleon divided by the DY cross section from pp scattering. Solid curves are predictions for RHIC ($\sqrt{s} = 200$ GeV) and dashed for LHC ($\sqrt{s} = 5.5$ TeV) Calculations are for the same kinematics as fig. 9.

For low transverse momenta, we expect DY dilepton production to be shadowed. Note that shadowing for longitudinal $q\bar{q}$ pairs is smaller than for transverse pairs because the longitudinal cross section is dominated by small distances in the dipole cross section. However, gluon shadowing, whose onset we observe in the RHIC predictions and which should become the dominant effect at LHC, is about the same for longitudinal and transverse pairs. Indeed, we predict rather different shadowing effects for longitudinal and transverse dileptons at RHIC, but about the same at LHC.

It is interesting that the effect of antishadowing, the so-called Cronin enhancement predicted in [12], disappears at the energy of RHIC after inclusion of gluon shadowing, which was disregarded in [12]. This reminds one of the missing Cronin enhancement in charged particle multiplicities that was measured at RHIC [43]. However, the RHIC data cannot be explained by gluon shadowing, because the x of these data is too large. Some antishadowing is still possible at large $q_T \sim 10$ GeV at the energy of LHC as a result of the substantial rise of the dipole cross section with energy and the corresponding relative enhancement of the multiple interactions responsible for the Cronin effect. This expectation is confirmed

by fig. 11, which shows the results of calculations with (solid curves) and without (dashed curves) gluon shadowing.

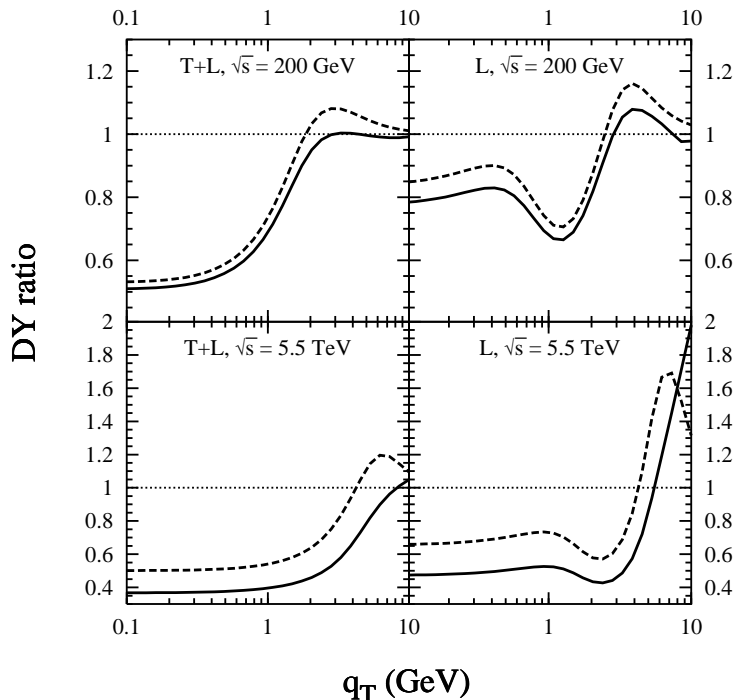


Figure 11: *The influence of gluon shadowing on the DY cross section. Dashed curves are calculated without gluon shadowing, i.e. $R_G = 1$ in (13), while solid curves include gluon shadowing. The influence on the longitudinal DY cross section is shown separately in the two left-hand plots (L). The two plots on the right show the DY ratio for the sum of the transverse and longitudinal cross sections (T + L). Calculations are for the same kinematics as fig. 9.*

The DY process with the production of a longitudinally polarized photon manifests stronger effects of antishadowing (fig. 10 bottom and fig. 11 right), as was earlier observed in [12]. However, this enhancement of the longitudinal cross section will be difficult to see in experiments because the transverse cross section is so much larger than the longitudinal one. All nuclear effects are expected to vanish at very large q_T .

One can also study the moments of the transverse momentum distribution. A frequently measured characteristic of nuclear effects is the broadening of the mean value of the DY transverse momentum squared, which is the difference between the values of mean transverse momentum squared measured in pA and pp collisions,

$$\delta\langle q_T^2 \rangle = \langle q_T^2 \rangle_A - \langle q_T^2 \rangle_N, \quad (20)$$

where

$$\langle q_T^2 \rangle_{A(N)} = \frac{\int_0^{q_T^{max}} d^2 q_T q_T^2 d\sigma_{DY}^{pA} / d^2 q_T}{\int_0^{q_T^{max}} d^2 q_T d\sigma_{DY}^{pN} / d^2 q_T}. \quad (21)$$

$d\sigma_{DY}^{pA} / d^2 q_T$ is the proton-nucleus DY cross section given by Eq. 16.

It is easy to understand from fig. 10 that a nuclear target leads to a larger mean transverse momentum of DY dileptons than a proton target: low q_T pairs, corresponding to large arguments of the dipole cross section ($\alpha\rho$), are shadowed, while high transverse momentum

pairs are not (color filtering [20]). However, the actual numerical value of broadening, i.e. the increase of the square mean transverse momentum, depends on the maximum q_T included in the analysis. This is not an artifact of our approach, as this is also the case in experiment.

According to (18) the numerator in (21) diverges at large q_T for the transverse cross section. Even after averaging over the projectile parton distribution, the integral is very slowly converging, and one has to introduce an upper cutoff q_T^{max} since there is a maximal transverse momentum accessible in experiment. On the other hand, the large- q_T tail of the differential cross section should be the same for nuclear and nucleon targets since no nuclear effects are expected at large q_T . For this reason one may think that the divergence would cancel in the difference in Eq. (20) and render the result cutoff independent. This might be true if no nuclear effects occurred in the integrated DY cross section, i.e. if $\sigma_{DY}^{pA} = A \sigma_{DY}^{pN}$. However this is never the case. For long coherence time, $t_c \gg R_A$, shadowing diminishes the DY nuclear cross section, i.e. the denominator in the first term in Eq. (20). As a result, the high- q_T tail of the nuclear q_T distribution is renormalized and undercompensated by the second term in Eq. (20). This is why there is sensitivity to the upper cutoff q_T^{max} in our results, and this sensitivity is even more pronounced at the higher energies where shadowing increases. On the other hand, for short $t_c \rightarrow 0$, where shadowing vanishes, energy loss has a similar effect of suppressing the DY cross section on nuclei [44, 2, 3].

Note that in at least some experiments [6, 45, 46], the transverse momentum broadening is extracted from the data by fitting the points with the functional form [47]

$$\frac{d\sigma_{DY}^{pA(N)}}{d^2q_T} = \frac{\sigma_0^{pA(N)}}{\left(1 + \frac{q_T^2}{(q_0^{pA(N)})^2}\right)^n}, \quad (22)$$

where typically $n = 6$ for both a proton and a nuclear target. The fast decay of the differential cross section in Eq. (22) is due to the increase of x_1 as function of q_T . As mentioned above, this effect vanishes at large x_F and high s . The q_T -distributions at RHIC and LHC (at large x_F) will be much flatter than (22).

In fig. 12 we compare A -dependences of the broadening $\delta\langle q_T^2 \rangle$ calculated with different cutoffs, $q_T^{max} = 5$ (bottom curves) and 10 GeV (upper curves). The main observations are first that broadening is roughly proportional to the path length in the nuclear medium. This is true for any value of q_T^{max} . Furthermore, $\delta\langle q_T^2 \rangle$ can become quite large for heavy nuclei, around 1 GeV at RHIC and around 3 GeV at LHC. While the influence of gluon shadowing on broadening is rather weak, the q_T^{max} -dependence is quite strong. This is studied in more detail in fig. 13. Increasing the transverse momentum cutoff from 5 GeV to 10 GeV at RHIC energy leads to an increase of nuclear broadening of slightly more than 50%. At LHC energies, however, where one still has nuclear effects in the transverse momentum distribution at rather large values of q_T , broadening increases by a factor of 3. Therefore, the DY process turns out to be a less than ideal tool to measure the broadening of the transverse momentum distribution for a quark propagating through nuclear matter.

Finally, we calculate the energy dependence of nuclear broadening, shown in the plot on the right in fig. 13. Again, calculations are performed for two different values of the transverse momentum cutoff. Note that the shape of the curve depends strongly on q_T^{max} .

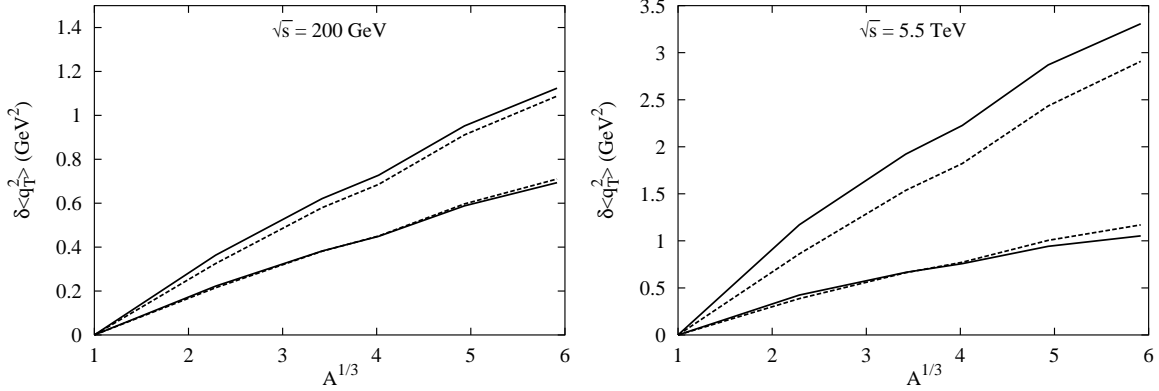


Figure 12: Nuclear broadening for DY dileptons from pAu at RHIC and LHC. Broadening depends on the transverse momentum cutoff q_T^{max} . In each plot, the lower pair of curves is calculated for $q_T^{max} = 5$ GeV, while the upper pair is for $q_T^{max} = 10$ GeV. The solid curves include gluon shadowing, the dashed ones do not. Calculations are for the same kinematics as fig. 9.

For a transverse momentum cutoff of 5 GeV, there is almost no energy dependence of $\delta\langle q_T^2 \rangle$ above RHIC energy. The situation looks different if the transverse momentum cutoff is 10 GeV. In this case, broadening does increase as function of energy. It will therefore be difficult to draw conclusions from possible future data on the energy dependence of $\delta\langle q_T^2 \rangle$, since presumably one will only see the cutoff dependence.

Valuable insight into the relationship between shadowing and broadening is gained if one performs the integration in the numerator of (21) analytically for $q_T^{max} \rightarrow \infty$. Without the projectile parton distribution, the result reads

$$\langle q_T^2 \rangle_{A(N)} = \eta^2 + \frac{C^{A(N)}(x_2)}{\sigma_{DY}^{qA(N)}(\alpha)} \int d^2\rho \left| \Psi_{\gamma^*q}^{T,L}(\rho, \alpha) \right|^2, \quad (23)$$

where the wave function squared has the form given in Eqs. (B.2) or (B.3); $\eta^2 = (1 - \alpha)M^2 + \alpha^2 m_q^2$; $\sigma_{DY}^{qA}(\alpha) = \int d^2q_T \sigma_{DY}^{qA}(q_T, \alpha)$; and

$$C^{A(N)}(x_2) = \left. \frac{\partial \sigma_{q\bar{q}}^{A(N)}(\rho, x_2)}{\partial \rho^2} \right|_{\rho \rightarrow 0}. \quad (24)$$

Note that without gluon shadowing, all the difference between a nucleus and a nucleon occurs in the denominator of the second term, $\sigma_{DY}^{qA(N)}(\alpha)$. Including gluon shadowing, one has

$$C^A(x_2) = C^N(x_2) \int d^2b R_G(x_2, b) T(b) = C^N(x_2) \left[A - \int d^2b \Delta R_G(x_2, b) T(b) \right]. \quad (25)$$

At the same time, the problem of the divergence at large q_T is moved to the integral of the LC wave function squared in the second term, which has logarithmic singularity at $\rho \rightarrow 0$.

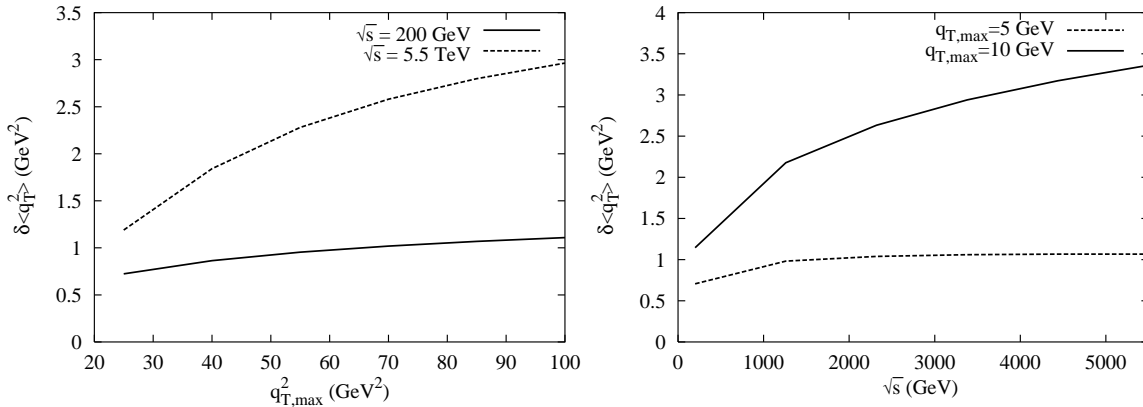


Figure 13: *The cutoff (left) and energy (right) dependence of transverse momentum broadening for pAu scattering. The calculations includes gluon shadowing. and are for the same kinematics as fig. 9.*

Thus, the broadening Eq. (20) takes the form,

$$\delta\langle q_T^2 \rangle = \left(\Delta R_{DY} - \frac{1}{A} \int d^2b \Delta R_G(x_2, b) T(b) \right) \frac{AC^N(x_2)}{\sigma_{DY}^{qA}(\alpha)} \int d^2\rho \left| \Psi_{\gamma^*q}^{T,L}(\rho, \alpha) \right|^2, \quad (26)$$

where ΔR_{DY} and ΔR_G are the nuclear suppressions for DY and for gluons, i.e. the difference from unity, $\Delta R_{DY} \equiv 1 - \sigma_{DY}^{qA}/(A\sigma_{DY}^{qN})$ (see Eq. 8 for ΔR_G).

We reach the interesting conclusion that if there is no shadowing, the broadening of the transverse momentum vanishes as well. This is a manifestation of a close relationship between broadening and shadowing in the regime of $t_c \gg R_A$. Indeed, broadening is interpreted in the LC dipole approach as color filtering. Namely, the mean size of a $q\bar{q}$ dipole that can be propagated through nuclear matter decreases with the size of the configuration; correspondingly, the intrinsic transverse momentum of the surviving configurations rises. Shadowing occurs due to the same phenomenon. Once one says that shadowing is negligibly small, this also means that the dipole is too small to undergo multiple interactions. However, in this case no color filtering occurs either. This rather intuitive result looks very nontrivial in the framework of parton model, where one can get broadening even without shadowing [48].

Note that gluon shadowing seems to reduce the amount of broadening in Eq. (26). This should be expected, since gluon shadowing reduces the nuclear thickness, cf. Eq. (13), and a more dilute medium leads to less broadening. However, shadowing for DY, ΔR_{DY} , increases with gluon shadowing. Numerically, we find that the influence of gluon shadowing cancels to a large extent and that broadening is almost independent of R_G , see Fig. 12.

In Eq. (21) we avoided the (logarithmic) divergence in $\langle q_T^2 \rangle$, related to the singular behavior of $K_1(\eta\rho)$ at small $\eta\rho$ for transverse photons, by introducing above an upper cutoff q_T^{max} on the integrals over q_T . These numerical results constitute quantitative predictions of the LC target rest frame formulation that may be compared to experiment noting that q_T^{max} is a physical parameter related to the acceptance of the spectrometer in the measurement.

Motivated by the desire to understand these same numerical results analytically, we next examine the theory employing certain simplifications and approximations.

Our main approximation is to make the replacement of the fluctuation distribution by a Gaussian,

$$|\Psi(\alpha, \rho)|^2 \rightarrow \frac{\alpha_{em}}{2\pi^2} ((1 + (1 - \alpha)^2) \eta^2 n^2 e^{-k_0^2 \rho^2}), \quad (27)$$

where $k_0^2 = 2\beta\eta^2$, with n^2 and β chosen to give an acceptable match to the actual fluctuation distribution, which we simplify to be

$$|\Psi(\alpha, \rho)|^2 = \frac{\alpha_{em}}{2\pi^2} ((1 + (1 - \alpha)^2) \eta^2 K_1^2(\eta\rho)), \quad (28)$$

noting that m_q is small and the longitudinal contribution is about a 10% correction to the momentum distribution. Because the distribution of fluctuations is integrable with the cutoff, the average size of the fluctuation is meaningful, and with the Gaussian wave function, the mean-square transverse spread of the fluctuation is $\langle \rho^2 \rangle = 1/k_0^2$.

With such approximations, the integral in Eq. (17) can be evaluated analytically. The result of carrying out the integrals over ρ_1 , ρ_2 , and q_T gives

$$\begin{aligned} \int d^2 q_T q_T^2 \frac{d^3 \sigma_{DY}^{qN}}{d(\ln \alpha) d^2 q_T} &\sim \pi \int d^2 b \left\{ \frac{2 C(\alpha) \alpha^2 T_A(b)}{k_0^2} + \frac{2 [C(\alpha) \alpha^2 T_A(b)]^2}{[2 k_0^2 + C(\alpha) \alpha^2 T_A(b)]^2} \right\} \\ &\approx \pi \int d^2 b \left\{ \frac{2 C(\alpha) \alpha^2 T_A(b)}{k_0^2} + \frac{[C(\alpha) \alpha^2 T_A(b)]^2}{2 k_0^4} + \dots \right\}, \end{aligned} \quad (29)$$

where we have omitted the prefactors in Eq. (27), and the expansion is useful for examining the limit of weak shadowing. Likewise,

$$\begin{aligned} \int d^2 q_T \frac{d^3 \sigma_{DY}^{qN}}{d(\ln \alpha) d^2 q_T} &\sim \frac{2\pi}{k_0^2} \int d^2 b \frac{C(\alpha) \alpha^2 T_A(b)}{2 k_0^2 + C(\alpha) \alpha^2 T_A(b)} \\ &\approx \pi \int d^2 b \left\{ \frac{C(\alpha) \alpha^2 T_A(b)}{k_0^4} - \frac{[C(\alpha) \alpha^2 T_A(b)]^2}{2 k_0^6} + \dots \right\}. \end{aligned} \quad (30)$$

In these expressions we have introduced an effective $C = C(\alpha)$, defined independent of β so that the Drell-Yan cross section for the GW color dipole cross section is reproduced in the ρ^2 approximation to it on a nucleon,

$$C(\alpha) = \frac{\int K_1^2(\eta\rho) \sigma(\alpha\rho) d^2\rho}{n^2 \int e^{-k_0^2 \rho^2} \alpha^2 \rho^2 d^2\rho}. \quad (31)$$

We could optimally match approximate theory to the exact one by choosing n^2 and β numerically for a given q_T^{max} , but since our interest is insight rather than numerical precision at this point our conditions are simply the following: (1) Preserve the integral $\int \rho^2 K_1^2(\eta\rho) d^2\rho$,

$$\int_0^\infty \rho^2 K_1^2(\eta\rho) d^2\rho = n^2 \int_0^\infty \rho^2 e^{-k_0^2 \rho^2} d^2\rho, \quad (32)$$

determining $n^2 = 16\beta^2/3$. (2) Adjust β to preserve $\langle\rho^2\rangle$ using the *asymptotic* form for $K_1(x)$. This gives $\beta = 1$. We determine the effective momentum cutoff corresponding to this Gaussian by comparing the exact numerical value for $\langle q_T^2 \rangle_N$ for the nucleon to the approximate value. The latter is obtained from the small- A limit of Eqs. (29) and (30),

$$\langle q_T^2 \rangle_N = 2\langle\alpha^2(1 + (1 - \alpha)^2)\rangle/\langle\alpha^2(1 + (1 - \alpha)^2)/k_0^2\rangle, \quad (33)$$

where the brackets indicate the convolution (16) with the quark distribution function. We find that for $q_T^{max} = 10$ GeV, $\langle q_T^2 \rangle_N$ agrees with the RHIC values to about 10% and LHC values to about 30%.

For a nucleus, the integrals over impact parameter in Eq. (29) and Eq. (30) may be carried out analytically for a sharp-surface density model in which the density is constant at ρ_0 out to radius $R_{1/2}$, and zero beyond. Then, from Eq. (29), we find

$$\int d^2q_T q_T^2 \frac{d^3\sigma_{DY}^{qN}}{d(\ln\alpha) d^2q_T} \sim \frac{4\pi^2 R_{1/2}^2}{y^2} \left[3\ln(1+y) + \frac{2}{3}y^3 + \frac{1}{2}y^2 - 2y - \frac{y}{1+y} \right]. \quad (34)$$

and from Eq. (30)

$$\int d^2q_T \frac{d^3\sigma_{DY}^{qN}}{d(\ln\alpha) d^2q_T} \sim \frac{4\pi^2 R_{1/2}^2}{y^2 k_0^2} \left[\ln(1+y) + \frac{y^2}{2} - y \right]. \quad (35)$$

where $y = C(\alpha)\alpha^2\rho_0 R_{1/2}/k_0^2$. To obtain $\langle q_T^2 \rangle$ for the nucleus, it is necessary to perform a convolution of these expressions with the quark distribution function of the nucleon projectile as in Eq. (16).

It is interesting to examine the expansion of Eq. (34) and Eq. (35) in powers of y . Recalling that $k_0^2 = 1/\langle\rho^2\rangle$, and further noting that $L = 2R_{1/2}$ is the diameter of the nucleus, this is essentially an expansion in $y = L/2\lambda$ where $\lambda = 1/\langle\sigma_{\bar{q}q}\rangle\rho_0$ is the mean-free path of the fluctuation. For most values of α , the number of interaction mean-free paths in crossing the nucleus is tiny due to the large value of M^2 in $\eta^2 = (1-\alpha)M^2 + \alpha^2 m_q^2$. However, for $\alpha \approx 1$, the mean transverse separation of the fluctuation may become relatively large (we find $\langle\rho^2\rangle^{1/2} = 0.7$ fm for $m_q = 0.2$ GeV). In fact, for a large nucleus ($A=208$), we see that for RHIC energies $C(\alpha \approx 1) = 2.5$ and $y \simeq 1.5$. Clearly, these larger fluctuations have a relatively small mean-free path λ and are subject to appreciable color filtering in traversing the nucleus. For LHC, $C(\alpha \approx 1) = 5.7$ and $y \simeq 3.4$. At the same time, the amount by which $\langle q_T^2 \rangle$ differs its value for a nucleon, Eq. (33), grows and hence nuclear broadening also grows. In this fashion, the physics of nuclear broadening is again seen to be directly related to color filtering for $\alpha \simeq 1$. Since the expansion of Eqs. (34) and (35) converges slowly in the region where the largest contributions to the nuclear broadening occur, it is necessary to evaluate the integrals over b and α without making an expansion to calculate $\delta\langle q_T^2 \rangle$ with sufficient accuracy.

With these approximations (we have also omitted gluon shadowing, which has been shown to have a weak effect on $\delta\langle q_T^2 \rangle$), we find for heavy nuclei $t_c \gg R_A$, $\delta\langle q_T^2 \rangle \propto \langle T_A^2 \rangle$, *i.e.* $\delta\langle q_T^2 \rangle$ is very nearly linear with $A^{1/3}$, just as we found in our more exact numerical

studies. The constants of proportionality are about $2.2C(x_2)$ at RHIC and $1.1C(x_2)$ at LHC, which overestimate the slope of the exact results by about 20% and 44%, respectively. Although linearity in $A^{1/3}$ would follow in the weak scattering limit, we again remark that our analytical calculations indicate substantial effects from higher-order multiple scattering.

In the opposite limit of short $t_c \rightarrow 0$, broadening of a quark is known to rise linearly with the length of the path of the quark in nuclear matter before the DY reaction occurs [49, 18],

$$\delta\langle q_T^2 \rangle_q = C(x_2) \langle T_A \rangle, \quad (36)$$

where $\langle T_A \rangle = \int d^2b T_A^2(b)/A$ is the mean nuclear thickness. At the same time, broadening for the DY pair, which carries only fraction α of the quark momentum, is reduced,

$$\delta\langle q_T^2 \rangle_{DY} = \langle \alpha^2 \rangle \delta\langle q_T^2 \rangle_q, \quad (37)$$

where

$$\langle \alpha^2 \rangle = \frac{\int_0^1 d\alpha \alpha^2 \int d^2\rho \left| \Psi_{q\gamma^*}(\rho, \alpha, M^2) \right|^2 \sigma_{q\bar{q}}^N(\rho, x)}{\int_0^1 d\alpha \int d^2\rho \left| \Psi_{q\gamma^*}(\rho, \alpha, M^2) \right|^2 \sigma_{q\bar{q}}^N(\rho, x)}. \quad (38)$$

This value depends on M logarithmically, and for $M \sim 5$ GeV, $\langle \alpha^2 \rangle \approx 0.9$.

It is interesting to compare the nuclear dependences of broadening in the two limiting regimes $t_c \gg R_A$, Eq. (26), and $t_c \rightarrow 0$, Eq. (36). Expanding the nuclear cross section Eq. (5) in $\sigma_{q\bar{q}}^N T_A(b)$, we can then perform the integration for longitudinal DY photons (for transverse photons it diverges). Then we arrive at the same expression Eq. (36), except that it acquires an extra factor

$$K = \frac{\langle [\sigma_{q\bar{q}}^N]^2 \rangle}{4 \left| \langle \sigma_{q\bar{q}}^N \rangle \right|^2}, \quad (39)$$

where

$$\langle \dots \rangle = \int d^2\rho (\dots) \left| \Psi_{\gamma^*q}^L(\rho, \alpha) \right|^2. \quad (40)$$

Applying the ρ^2 approximation Eq. (10) for the dipole cross we get $K = 4/5$. Thus, the broadening for longitudinal DY pairs in the asymptotic regime $t_c \gg R_A$ matches rather well the low energy regime.

The dependence of the broadening $\delta\langle q_T^2 \rangle$ on the cut-off is an unpleasant property that brings uncertainty to the comparison of theory with data. As we mentioned, it is related to the large q_T behavior Eq. (18) of the DY cross section, leading to a logarithmic divergence in the integral over q_T weighted with q_T^2 ,

$$\langle \sigma_{DY}^{pA} q_T^2 \rangle \equiv \int_0^{q_T^{max}} d^2q_T q_T^2 \sigma_{DY}^{pN}(q_T, \alpha), \quad (41)$$

which is the numerator in (21). Since this integral has exactly the same divergence at large q_T^{max} for nuclear and nucleon targets, it must cancel in the difference,

$$\delta\langle \sigma_{DY} q_T^2 \rangle = \langle \sigma_{DY}^{pA} q_T^2 \rangle - A \langle \sigma_{DY}^{pN} q_T^2 \rangle, \quad (42)$$

and the result should be independent of the upper cut-off q_T^{max} when it is sufficiently large. One can also normalize this difference dividing both terms by $A \langle \sigma_{DY} \rangle$. Unfortunately, the result is not an exact measure of the broadening of the transverse momentum of a quark propagating through a nucleus. However, these quantities are independent of the experimental acceptance (q_T^{max}), and this fact makes it a better observable than the broadening, Eq. (20), to compare with theory.

6 Polarization of DY pairs

In the preceding section, we separately calculated the DY cross section for transverse and longitudinal photons. In experiment, the different polarizations can be distinguished by investigating the angular distribution of DY pairs. The most general form of the DY angular distribution reads [21],

$$\frac{d^4\sigma}{dx_F dM^2 d\cos\theta d\phi} \propto 1 + \lambda \cos^2\theta + \mu \sin(2\theta) \cos(\phi) + \frac{\nu}{2} \sin^2(\theta) \cos(2\phi), \quad (43)$$

where θ is the angle between the muon and the z -axis in the rest frame of the virtual photon, and ϕ is the azimuthal angle. Of course, λ and ϕ depend on the choice of z -axis in the dilepton center-of-mass frame. Since the dipole approach is formulated in the target rest frame, it is convenient to put the z -axis in the direction of the radiated photon [11]. The target rest frame and the dilepton center-of-mass frame are then related by a boost in z -direction, so that the transverse polarizations are the same in the target rest frame and in the photon rest frame. Note that in the dilepton center-of-mass frame, the z -axis is antiparallel to the target momentum. This frame is called the u -channel frame and the curves we present are valid in this frame.

The ϕ -dependence of the cross section is difficult to measure. At RHIC, only the value of λ can be measured [45]. Since $\lambda = +1$ for transverse and $\lambda = -1$ for longitudinal, one obtains after integration over the azimuthal angle,

$$\lambda = \frac{\sigma_T - \sigma_L}{\sigma_T + \sigma_L}. \quad (44)$$

Our results for λ as function of q_T at RHIC and LHC energies are shown in fig. 14. Note that $q_T^2 = x_1 x_2 S - M^2$ is a Lorentz invariant variable and therefore has the same value for all choices of the z -axis. At low q_T , λ shows a clear deviation from unity. This deviation increases with energy, because the longitudinal cross section is more strongly dominated by small distances than the transverse. Since the dipole cross section grows faster with energy at small separations, the relative amount of longitudinal photons at small q_T increases with energy, see fig. 9. At very large transverse momentum, λ will eventually approach unity because the longitudinal cross section falls off steeper than the transverse one (18). It is also interesting to investigate nuclear effects on λ . For pp collisions, λ has been calculated previously in [13]. One sees from fig. 14, that the nucleus leads to a stronger suppression at small q_T than a proton target. This is because longitudinal photons are less shadowed

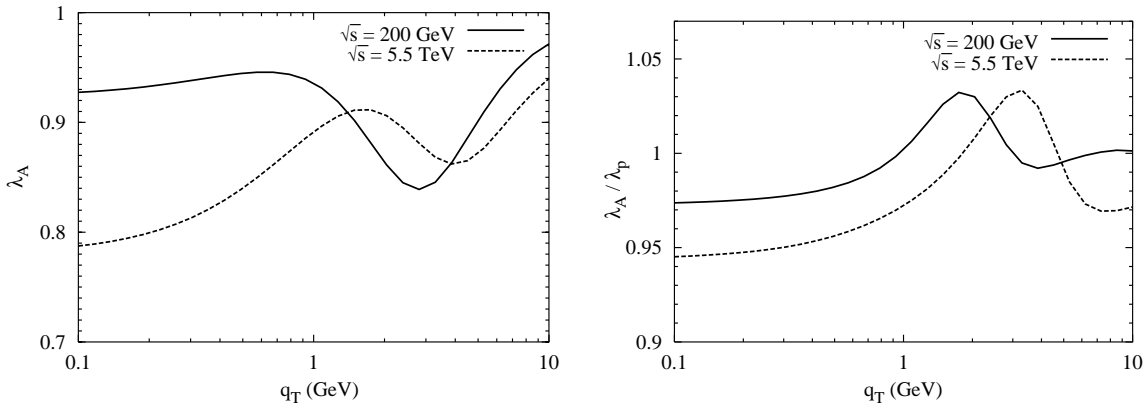


Figure 14: *The parameter λ (44) in D Au collisions at RHIC and LHC (left). The figure on the right illustrates nuclear effects on λ , by showing the ratio of λ for D Au scattering and for pp scattering. Calculations are for the same kinematics as in fig. 9 and include gluon shadowing.*

at $q_T \rightarrow 0$ than transverse, fig. 10. Nuclear effects on λ vanish at very large transverse momentum, as expected.

An interesting feature of our result is that the parton model relation

$$1 - \lambda - 2\nu = 0, \quad (45)$$

which is known as Lam-Tung relation [21], is not fulfilled in the dipole approach. The violation of the Lam-Tung relation becomes apparent from the behavior of λ as $q_T \rightarrow 0$. Kinematics require that the double-spin-flip amplitude ν vanishes at $q_T = 0$, thus λ should approach unity. Remarkably, this relation holds to order α_s in the QCD improved parton model. Note that (45) even holds separately for the annihilation and for the Compton corrections in the parton model. Even at order α_s^2 , the corrections to (45) are very small [50], by order of magnitude $1 - \lambda - 2\nu \sim 10^{-2}$. Experimentally, the Lam-Tung relation is clearly violated [51], $1 - \lambda - 2\nu \sim -1$. However, all experimental data lie at large x_2 and are therefore not relevant for our calculation. At present, the reason for the violation of (45) is not known. Possibly, higher twist effects, included by default in our dipole approach, can provide an explanation [52]. However, it is not yet possible to apply the resummation technique [53] for logs in (q_T/M) to higher twists, which would be necessary to compare to future data on DY angular distributions from PHENIX.

The dipole formulation provides a much easier way to calculate the DY transverse momentum distribution even at low q_T . It is not surprising that the result from the $\mathcal{O}(\alpha_s)$ parton model calculation is not reproduced in our approach, because the dipole picture is not an expansion in powers of the strong coupling constant. Instead, all contributions from higher order graphs that are enhanced by a large $\log(1/x_2)$ are contained in the dipole cross section. Moreover, if we use a phenomenological parameterization of $\sigma_{q\bar{q}}^N$, some higher twists and nonperturbative effects are contained as well. The Lam-Tung relation is violated in our calculation because of the flattening of the dipole cross section. Indeed, for a quadratically

rising $\sigma_{q\bar{q}}^N(\rho, x) = C(x)\rho^2$, λ would vanish at $q_T = 0$, as can be seen from (17). Note that the remaining coefficients for the DY angular distribution (43) in the dipole formulation can be obtained from Eqs. (22)-(25) of [11]. It is easy to check that (45) is fulfilled only with $\sigma_{q\bar{q}}^N(\rho, x) = C(x)\rho^2$. Thus, the Lam-Tung relation is also violated in pp -collisions [13]. Finally, we would like to stress that the behavior of λ at low q_T depends heavily on the large ρ behavior of the dipole cross section, which is not well constrained by DIS and diffractive data. However, even if (7) is unrealistic at large separations, the qualitative behavior of λ will remain the same for any flattening parameterization. We therefore believe that it is worthwhile to measure λ at RHIC, because such data could give us information about the dynamics beyond the conventional parton model.

7 DY process in heavy ion collisions

As we pointed out in the introduction it is impossible to predict nuclear shadowing for the DY process in nuclear collisions from the parton model using data for DIS and the DY reaction on proton and nuclear targets. Indeed, the nuclear effects to be predicted are presented in the form,

$$R_{DY}^{AB}(x_1, x_2) \equiv \frac{\sigma_{DY}^{AB}(x_1, x_2)}{AB \sigma_{DY}^{NN}(x_1, x_2)}, \quad (46)$$

where

$$\begin{aligned} \sigma_{DY}^{AB}(x_1, x_2) &= N \sum_f Z_f^2 \int d^2b \int d^2s T_A(\vec{s}) T_B(\vec{b} - \vec{s}) \left[q_f^v(x_1) R_v^A(x_1, \vec{s}) \bar{q}_f^s(x_2) R_s^B(x_2, \vec{b} - \vec{s}) \right. \\ &\quad + \bar{q}_f^s(x_1) R_s^A(x_1, \vec{s}) q_f^v(x_2) R_v^B(x_2, \vec{b} - \vec{s}) + q_f^s(x_1) R_s^A(x_1, \vec{s}) \bar{q}_f^s(x_2) R_s^B(x_2, \vec{b} - \vec{s}) \\ &\quad \left. + \bar{q}_f^s(x_1) R_s^A(x_1, \vec{s}) q_f^s(x_2) R_s^B(x_2, \vec{b} - \vec{s}) \right], \quad (47) \end{aligned}$$

$$\begin{aligned} \sigma_{DY}^{NN}(x_1, x_2) &= N \sum_f Z_f^2 \left[q_f^v(x_1) \bar{q}_f^s(x_2) + \bar{q}_f^s(x_1) q_f^v(x_2) \right. \\ &\quad \left. + q_f^s(x_1) \bar{q}_f^s(x_2) + \bar{q}_f^s(x_1) q_f^s(x_2) \right], \quad (48) \end{aligned}$$

and \vec{b} is the impact parameter of the beam (A) and target (B) nuclei. The first two terms in Eq. (47) correspond to (i) annihilation of a valence quark of the beam with a sea antiquark of the target; (ii) a sea antiquark of the beam with a valence quark of the target. The third and fourth terms correspond to (iii) both the quark and antiquark originating from either the sea of the beam or target. Provided that the Drell-Yan K -factor is independent of A and B , the overall normalization factor N in these expressions is irrelevant for shadowing Eq. (46) since it cancels in the ratio. This assumption is supported by experimental data on the K factor for various heavy ion collisions [54].

Note that a generalization of Eqs. (16) – (17) to the case of AB scattering including higher twist effects, would be much more complicated than Eqs. (47) – (48). Such higher twist effects, however, will be important only for nuclear effects in the DY transverse momentum distribution in AB , which are beyond the scope of this paper.

All parton distributions in Eqs. (47) – (48) are taken at the same virtuality $Q^2 = M^2$. For the sake of simplicity, we assume that the shadowing, R_s^A , is the same for sea quarks and antiquarks, and we neglect the isospin noninvariance of the sea distribution at moderately small $x \sim 0.1$ [55], which can easily be taken into account.

The nuclear shadowing $R_{q_1}^A(x, \vec{s})$ is given in Sect. 7.1 below. Note that $R_q^A(x, b)$ at small x is a function of nuclear thickness. It vanishes at large impact parameters on the nuclear periphery, but it reaches its maximum at $b = 0$. Data for DIS or the DY reaction in pA collisions provide information only about the b -integrated shadowing effect. Knowledge of only such integrated shadowing is not sufficient for the calculation of shadowing in an AB collision, Eq. (47). Nevertheless, it was assumed in [8] that shadowing is independent of impact parameter, $R_q^A(x, Q^2, b) = R_q^A(x, Q^2)$. Clearly, such an *ad hoc* assumption is not justified and leads to basic consequences which cannot be accepted. For instance, it precludes any dependence of shadowing effects on centrality in heavy ion collision.

As we demonstrated above, the LC dipole approach provides direct access to the impact parameter dependence of shadowing effects. In the following subsection, we calculate shadowing for valence and sea quarks and compare the b -integrated result to the EKS98 parameterization [4]. Of course, the impact parameter dependence of shadowing is taken into account in Sect. 7.2, where we predict shadowing for the DY reaction in a nuclear collision in the integrated form Eq. (47), as well as a function of centrality. In order to calculate $R_{DY}^{AB}(x_1, x_2, b)$ for a collision with impact parameter b , one should just eliminate the integration over \vec{b} in the numerator of Eq. (47), and replace

$$AB \Rightarrow T_{AB}(b) = \int d^2s T_A(s) T_B(\vec{b} - \vec{s}) \quad (49)$$

in the denominator of Eq. (46). Comparison with the minimal-bias events for DY dilepton production in heavy ion collisions would serve as a rigorous test of the theory.

7.1 Nuclear shadowing for sea and valence quarks

Since we rely on the factorization relations Eqs. (46) – (48), we can calculate shadowing $R_s^A(x, Q^2)$ and $R_v^A(x, Q^2)$ in DIS, which looks somewhat simpler as it does not include a convolution with the initial quark distribution.

Shadowing for sea quarks is calculated with Eq. (13) and is given by

$$R_s(x, Q^2, b) = \frac{2 \int_0^1 d\alpha \int d^2\rho \left| \Psi_{q\bar{q}}(\rho, \alpha, Q^2) \right|^2 \left[1 - \left(1 - \frac{1}{2A} \sigma_{q\bar{q}}^N(\rho, x) R_G(x, \lambda/\rho^2, b) T_A(b) \right)^A \right]}{T_A(b) \int_0^1 d\alpha \int d^2\rho \left| \Psi_{q\bar{q}}(\rho, \alpha, Q^2) \right|^2 \sigma_{q\bar{q}}^N(\rho, x)} \quad (50)$$

The light-cone wavefunctions $\Psi_{q\bar{q}}$ for the transition $\gamma^* \rightarrow q\bar{q}$ can be found in the literature, see *e.g.* [17]. Let us recall that this expression is valid only for the so-called “frozen” approximation, i.e. in the asymptotic regime $t_c \gg R_A$, which takes place at very small x . In the transition region $t_c \lesssim R_A$ one should employ the LC Green function technique. This was done in [56, 39], although gluon shadowing was neglected in those calculations. At very

small x gluon shadowing is essential, as demonstrated above (see comparison with data from the NMC experiment in [3]).

Nuclear shadowing for valence quarks has never been calculated. This shadowing is usually believed to be small [4], if it occurs at all. We shall demonstrate, however, that shadowing for valence quarks is quite sizable, even stronger than the shadowing of sea quarks. This is another new result of the present paper. We note in this regard that the nuclear structure function $F_2(x)$ is different from the quark distribution function in an essential way; namely, the former contains shadowing effects and therefore the baryon number sum rule is not applicable to it [24], a difference that may explain the discrepancy of our results compared to Ref. [4].

Note that we call the ratio Eq. (50) shadowing for sea quarks because the dipole cross section $\sigma_{q\bar{q}}^N(\rho, x)$ includes only the part that rises with energy, corresponding to gluonic exchanges in the cross-channel. Therefore, this is the part of the sea generated via gluons (there are also other sources of the sea, for instance the meson cloud of the nucleon, but they vanish linearly with x or faster). The fact that the color-dipole cross section includes only the part generated by gluons is the reason why it should be used only at very small $x < 0.01$, where the sea dominates. This part of the dipole cross section can be called the Pomeron in the language of Regge phenomenology. In the same framework, one can relate the valence quark distribution in the proton to the Reggeon part of the dipole cross section, which has been neglected so far.

Thus, to include valence quarks in the dipole formulation of DIS, one should replace

$$\sigma_{q\bar{q}}^N(\rho, x) \Rightarrow \sigma_{q\bar{q}}^{\mathbf{P}}(\rho, x) + \sigma_{q\bar{q}}^{\mathbf{R}}(\rho, x) , \quad (51)$$

where the first (Pomeron) term corresponds to the gluonic part of the cross section, which we have used so far. It is responsible for the sea quark part of the nucleon structure function. The second (Reggeon) term must reproduce the distribution of valence quarks in the nucleon; this condition constraints its behavior at small x . One can guess that it has the following form,

$$\sigma_{q\bar{q}}^{\mathbf{R}}(\rho, x) = \tilde{N} \rho^2 \sqrt{x} , \quad (52)$$

where \sqrt{x} should reproduce the known x dependence of valence quark distribution (as, in fact, motivated by Regge phenomenology), and the factor ρ^2 is needed to respect the Bjorken scaling. The factor \tilde{N} will cancel in what follows.

We are now in a position to calculate shadowing for valence quarks by inserting the cross section Eq. (51) into the eikonal expression Eq. (50). Clearly, only the gluonic part of the dipole cross section is subject to gluon shadowing, i.e. only the first (Pomeron) term of Eq. (51) should be multiplied by R_G . Furthermore, if one expands the numerator in powers of $\sigma_{q\bar{q}}^{\mathbf{R}}$ and picks out the linear term⁴, then one arrives at the following expression for nuclear

⁴The small size of $\sigma_{q\bar{q}}^{\mathbf{R}}(\rho, x)$ at small x motivates such an expansion; however, one should note that it would not be proper to include the higher powers of the Reggeon cross section. Indeed, the Reggeons correspond to planar graphs. These cannot be eikonalized since they lead to the so-called AFS (Amati-Fubini-Stangellini) planar graphs, which vanish at high energies [33].

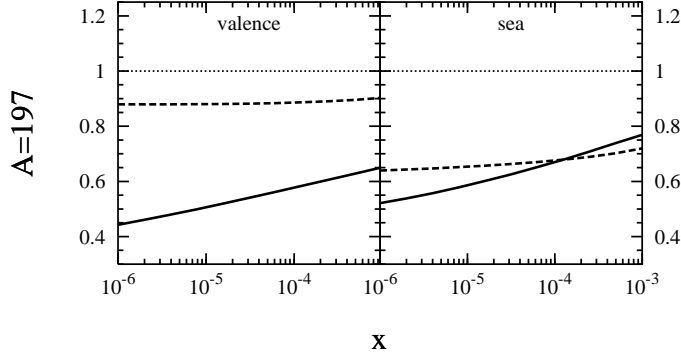


Figure 15: *Shadowing for sea and valence u -quarks in DIS off gold at $Q = 4.5$ GeV. Solid lines are calculated from Eqs. (55) – (56), while dashed curves show the EKS98 parameterization [4].*

shadowing of the valence quarks,

$$R_v(x, Q^2, b) = \frac{\int_0^1 d\alpha \int d^2\rho \left| \Psi_{q\bar{q}}(\rho, \alpha, Q^2) \right|^2 \sigma_{q\bar{q}}^{\mathbf{R}}(\rho, x) \left[1 - \frac{1}{2A} \sigma_{q\bar{q}}^{\mathbf{P}}(\rho, x) R_G(x, \lambda/\rho^2, b) T_A(b) \right]^A}{\int_0^1 d\alpha \int d^2\rho \left| \Psi_{q\bar{q}}(\rho, \alpha, Q^2) \right|^2 \sigma_{q\bar{q}}^{\mathbf{R}}(\rho, x)}. \quad (53)$$

This shadowing is even stronger than the shadowing for sea quarks, Eq. (50). Indeed, for weak shadowing we can also expand Eqs. (50) and (53) in powers of $\sigma_{q\bar{q}}^{\mathbf{P}}$. Then one obtains a shadowing correction $1 - R_v = \frac{1}{2} \sigma_{eff} T_A$ in (53) which is twice as large as that for sea quarks $1 - R_s = \frac{1}{4} \sigma_{eff} T_A$ in (50). Here $\sigma_{eff} = \langle \sigma_{q\bar{q}}^2 \rangle / \langle \sigma_{q\bar{q}} \rangle$ [3].

These estimates rely, however, on the ρ^2 -approximation for the dipole cross section and on the assumption that shadowing is weak. The result of our calculation, including gluon shadowing and a realistic parameterization (7) of the dipole cross section, is shown in fig. 15. We show only the b -integrated shadowing, which is given by

$$R_v(x, Q^2) = \frac{\int d^2b T_A(b) \int_0^1 d\alpha \int d^2\rho \left| \Psi_{q\bar{q}}(\rho, \alpha, Q^2) \right|^2 \sigma_{q\bar{q}}^{\mathbf{R}}(\rho, x) \left[1 - \frac{1}{2A} \sigma_{q\bar{q}}^{\mathbf{P}}(\rho, x) R_G(x, \lambda/\rho^2, b) T_A(b) \right]^A}{A \int_0^1 d\alpha \int d^2\rho \left| \Psi_{q\bar{q}}(\rho, \alpha, Q^2) \right|^2 \sigma_{q\bar{q}}^{\mathbf{R}}(\rho, x)} \quad (54)$$

for valence quarks and by

$$R_s(x, Q^2) = \frac{2 \int d^2b \int_0^1 d\alpha \int d^2\rho \left| \Psi_{q\bar{q}}(\rho, \alpha, Q^2) \right|^2 \left[1 - \left(1 - \frac{1}{2A} \sigma_{q\bar{q}}^N(\rho, x) R_G(x, \lambda/\rho^2, b) T_A(b) \right)^A \right]}{A \int_0^1 d\alpha \int d^2\rho \left| \Psi_{q\bar{q}}(\rho, \alpha, Q^2) \right|^2 \sigma_{q\bar{q}}^N(\rho, x)}. \quad (55)$$

for sea quarks. Shadowing for valence quarks is still stronger than it is for sea quarks, but not by a factor of 2. However, valence quark shadowing calculated in the LC approach is much stronger than in the parameterization of [4]. Note that the authors of [4] force their fit to the

nuclear valence quark distribution to fulfill the baryon number sum rule, which is however violated by shadowing effects. Therefore valence quark shadowing is underestimated in [4].

Unfortunately, it will be impossible to extract the low- x valence quark distribution of a nucleus from DY experiments, because the nuclear structure function is dominated by sea quarks. Maybe neutrino-nucleus scattering experiments could provide data that help to differentiate shadowing for sea and valence quarks.

7.2 Modification of the DY cross section in heavy-ion collisions

We can now make use of Eqs. (46) – (48) and predict nuclear effects for the cross section of DY lepton pair production in heavy ion collisions. We perform calculations at large x_F , where the structure function of the target nucleus, say nucleus B in (47), enters at small $x_2 \ll 0.1$ and is therefore subject to shadowing. We calculate the shadowing ratios $R_{s,v}$ in (47) as function of impact parameter from Eqs. (50) and (53). However, shadowing considered in the previous section is not the only nuclear effect affecting the ratios $R_{s,v}(x_1, x_2)$. Indeed, the parton distributions of the projectile nucleus, A , are sampled at $x_1 \gtrsim 0.1$, i.e. in the region where the EMC [57] effect must be taken into account. This leads to a 10 – 20% suppression at medium-large x_1 and a strong enhancement at $x_1 \approx x_F \rightarrow 1$ due to Fermi motion. Also, a small 2 – 3% enhancement is known to exist at $x_1 \sim 0.1$. All these are medium effects caused by the difference between the properties of bound and free nucleons. Since the nuclear density, apart from its surface, is approximately the same for all nuclei except for the lightest ones, one can assume that these medium effects are about the same for all bound nucleons in all nuclei. This assumption is supported by data, which displays no strong A -dependence of the EMC effect from medium through heavy nuclei [57]. Of course, there is no contradiction here with our previous statement about a strong impact parameter dependence of nuclear shadowing.

For our actual calculations, we employ the EKS98 [4] parameterization of the nuclear parton distributions for nuclear effects at large x (EMC, Fermi motion). For the parton densities of a proton, which are needed as a baseline for EKS98 and for calculation of the denominator (48), we use the CTEQ5L parameterization [40]. Note that, unlike in the pA case, parton densities of the proton are not only needed at large x , but also at very small $x \ll 0.1$. The CTEQ parameterization is applicable down to $x = 10^{-5}$, which is sufficient for RHIC ($x_2 \approx 0.001$) but not for LHC, where values as low as $x \approx 10^{-6}$ are reached. For the LHC calculation, we therefore switch to GRV98LO [58], which is applicable down to $x = 10^{-9}$. All evolution codes are taken from CERNLIB PDFLIB 8.04 [41].

Our predictions for the DY modification in AA collisions at RHIC and LHC are shown in fig. 16. For comparison, we also display the analogous curves for pA scattering from Sect. 4. The plot on the left shows that DY dilepton production in $AuAu$ collisions is suppressed much more strongly than in pAu collisions at the same kinematics, except for large values of x_F , where Fermi motion makes the nuclear suppression vanish. However, the strong suppression in $AuAu$ collisions is not just a combination of shadowing and the EMC effect. As one can see from the plot on the right, DY from $AuAu$ is still suppressed by about 40% compared to pp at very large b , where such nuclear effects are absent. Indeed, a nonnegligible

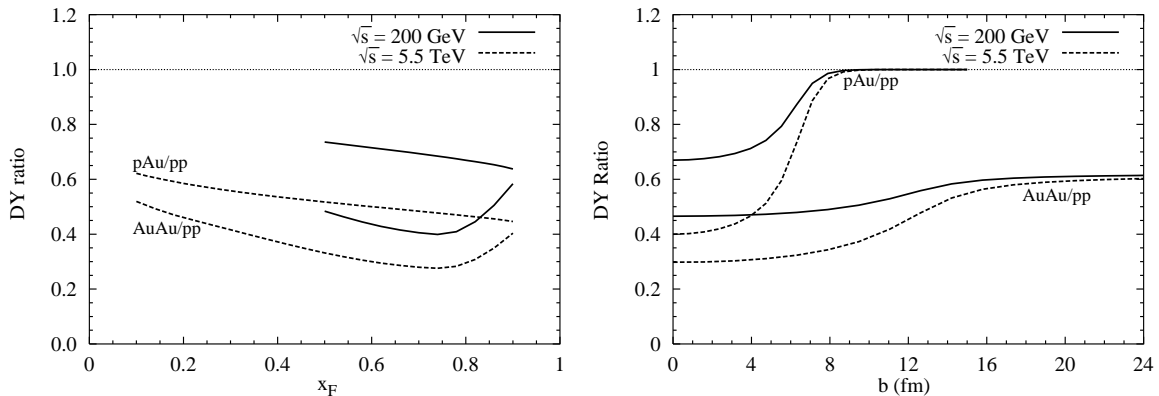


Figure 16: *Nuclear effects on the DY process in heavy ion collisions at $M = 4.5$ GeV. For comparison, the corresponding curves for pAu scattering (fig. 7) are also displayed. The plot on the right, which shows the impact parameter dependence of nuclear effects, is calculated at $x_F = 0.5$. The curves for AuAu collisions do not approach 1 at large b because of the different flavor composition of a nucleus. Note that all curves are divided by the values for pp scattering.*

part of the suppression in nucleus-nucleus collisions is due to the different flavor composition of nuclei. A heavy nucleus like gold ($A = 197$, $Z = 79$) has more neutrons than protons, thus the average nucleon in this nucleus has an excess of d -quarks over u -quarks, compared to a proton. Since d -quarks enter the lowest-order expression for the DY cross section (48) with a weight factor of $Z_d^2 = 1/9$ (compared to $Z_u^2 = 4/9$) one observes an additional suppression. Finally, we mention that the suppression at large b could be even stronger than in fig. 16, because neutrons are predominantly located at large impact parameter. This effect is not taken into account in our calculation, where all nucleons are assumed to be uncorrelated.

8 Summary and outlook

We have presented an analysis of nuclear effects in DY dilepton production in pA and AB collisions. All calculations are performed within the light cone dipole formalism for the DY process, because this approach suggests a very simple and intuitive treatment of nuclear effects. It essentially simplifies at high energies, where the coherence length for the DY process substantially exceeds the nuclear size. Then one can employ the eikonal formalism to describe multiple interactions, since the different eigenstates of interaction do not mix. This regime, relevant to the energies of RHIC and LHC, is considered throughout the paper. Formulas for the DY cross section are sufficiently simple to incorporate realistic nuclear densities and a realistic parameterization of the dipole cross section. The predictions for RHIC and LHC presented here can therefore be compared to future data and serve as a test of the theory.

Since we assume the coherence length to be long, gluon shadowing becomes important. The coherence length for higher Fock states is shorter than that for the lowest Fock state, and it is usually the order of, or shorter than, the nuclear radius. In this case, simple eikonalization cannot be applied to gluon shadowing and we employ the LC Green function formalism, which takes account of the variations in size of the projectile fluctuations as they propagate through the nucleus. The gluon shadowing incorporated in our calculations is especially important at very high energies, or small $x_2 \ll 1$, and it makes the $q\bar{q}$ -nucleus cross section saturate at a value significantly smaller than the geometrical limit of $2\pi R_A^2$.

Not surprisingly, gluon shadowing leads to a stronger suppression of the total DY cross section than one would obtain from quark shadowing alone. Note that while fixed target experiments at medium-high energies find suppression of the DY cross section only at large Feynman- x_F , partially caused by onset of shadowing and energy loss, we expect the entire $x_F > 0$ -range shadowed at RHIC and LHC. For the DY transverse momentum distribution, gluon shadowing leads to nontrivial modifications. At low lepton-pair transverse momentum, gluon shadowing enhances the suppression already expected from quark shadowing, but at intermediate transverse momentum, it strongly reduces the enhancement from the Cronin effect. This observation resembles the missing Cronin enhancement in charged particle multiplicities [43]. However, the latter effect cannot be due to gluon shadowing, because the x of the data is too large. The observed nuclear suppression is probably caused by final state interactions with the produced matter and is related to the induced energy loss and absorption. This will be studied in more detail in a forthcoming publication.

Furthermore, we calculate the nuclear broadening of the mean transverse momentum squared for DY dileptons produced in pA collisions. This quantity turns out to be divergent for radiation of transversely polarized DY photons. We demonstrate that this problem is caused by nuclear shadowing in the total DY cross section and that the two phenomena, broadening and shadowing, are closely related. As a result, the predicted broadening of the transverse momentum squared depends strongly on the upper cutoff on q_T . This is not purely a problem of the theoretical approach, as this cutoff dependence is present also in the experimental analysis. We found that $\langle \delta q_T^2 \rangle$ can vary up to a factor of three, depending on the cutoff. We suggest a different observable in which the divergent tails of the q_T distribution cancel and therefore render the result independent of the cutoff.

We separately analyze the differential DY cross sections for transversely and longitudinally polarized pairs. In both cases, the differential cross section $d\sigma/d^2q_T$ does not diverge as $q_T \rightarrow 0$. This result follows naturally in the dipole approach as a consequence of the saturating dipole cross section. In the parton model, a more complicated resummation of logs in q_T/M is necessary in order to render the DY cross section finite as $q_T \rightarrow 0$. On the partonic level and for large transverse momenta, we reproduce the behavior expected from perturbative QCD, namely $d\sigma_T/d^2q_T \propto q_T^4$ for transverse pairs and $d\sigma_L/d^2q_T \propto q_T^6$ for longitudinal.

Experimentally, the transverse and the longitudinal DY cross sections can be distinguished by investigating the angular distribution of DY pairs. We calculate the parameter λ , Eq. (44), which characterizes the relative contribution of transverse and longitudinal pairs to the DY cross section as a function of the dilepton transverse momentum and, in addition,

investigate nuclear effects on λ . Although these nuclear effects do not turn out to exceed 6%, the different q_T -dependence of the transverse and longitudinal cross sections leads to a nonmonotonic behavior of λ that can be observed in future experiments.

Finally, we present estimates for nuclear effects in heavy ion collisions at the energies of RHIC and LHC. We make use of QCD factorization, but calculate nuclear shadowing for sea and valence quarks separately within the LC dipole approach. Contrary to usual expectations, we found considerable shadowing for valence quarks, stronger than for sea quarks. We calculate nuclear suppression of DY dilepton production for $AuAu$ collisions as function of x_F and impact parameter b and find considerably stronger suppression in $AuAu$ collisions than in pAu collisions. Even at large impact parameter, the nucleus-nucleus DY cross section is reduced compared to pp as a result of flavor effects.

We leave for further study the following problems: (i) Since the approximation of a long coherence length employed for the DY process at RHIC is satisfied only at $x_F \gtrsim 0.5$, one must use the LC Green function technique in order to cover the entire range of x_F . It can also provide a proper interpretation for the Fermilab data [1]. (ii) Development of the LC dipole approach for the DY process in heavy ion collisions is still a challenge; (iii) Nuclear modification of the transverse momentum distribution and polarization effects should be also calculated for nucleus-nucleus collisions.

Acknowledgments: We are grateful to Jen-Chieh Peng for informing us about details of experiments and for useful discussions. B.Z.K. thanks the High Energy and Nuclear Theory groups at Brookhaven National Laboratory for hospitality during his visit when the present paper was completed. J.R. is grateful to Rainer Fries and Arthur Hebecker for discussion on the Lam Tung relation. This work was partially supported by the Gesellschaft für Schwerionenforschung Darmstadt (GSI), grant GSI-OR-SCH, and by the U.S. Department of Energy at Los Alamos National Laboratory under Contract No. W-7405-ENG-38.

Appendix A Calculation of gluon shadowing

Gluon shadowing is given by the shadowing for longitudinal photons as

$$R_G(x, Q^2) = \frac{G_A(x, Q^2)}{AG_N(x, Q^2)} \equiv 1 - \frac{\Delta\sigma_L^{\gamma^*A}(x, Q^2)}{A\sigma_L^{\gamma^*p}(x, Q^2)}. \quad (\text{A.1})$$

and is calculated according to the formulas derived in [29]. In this appendix, we give some details of our calculation. Our starting point is Eq. (90) of [29]:

$$\Delta\sigma_L^{\gamma^*A}(x, Q^2) = \int d^2b \int_{-\infty}^{\infty} dz_1 \int_{-\infty}^{\infty} dz_2 \Theta(z_2 - z_1) \rho_A(b, z_1) \rho_A(b, z_2) \Gamma(x, Q^2, z_2 - z_1) \quad (\text{A.2})$$

where

$$\Gamma(x, Q^2, \Delta z) = \Re \int d \ln(\alpha_G) \frac{16\alpha_{em} (\sum_F Z_q^2) \alpha_s(Q^2) C_{eff}^2}{3\pi^2 Q^2 \tilde{b}^2}$$

$$\begin{aligned}
& \times [(1 - 2\zeta - \zeta^2)e^{-\zeta} + \zeta^2(3 + \zeta)E_1(\zeta)] \\
& \times \left[\frac{t}{w} + \frac{\sinh(\Omega\Delta z)}{t} \ln\left(1 - \frac{t^2}{u^2}\right) + \frac{2t^3}{uw^2} + \frac{t \sinh(\Omega\Delta z)}{w^2} + \frac{4t^3}{w^3} \right] \quad (\text{A.3})
\end{aligned}$$

is given by Eq. (112) of [29] and

$$\Delta z = z_2 - z_1, \quad (\text{A.4})$$

$$\Omega = \frac{iB}{\alpha_G(1 - \alpha_G)\nu}, \quad (\text{A.5})$$

$$B = \sqrt{\tilde{b}^4 - i\alpha_G(1 - \alpha_G)\nu C_{eff}\rho_A}, \quad (\text{A.6})$$

$$\nu = \frac{Q^2}{2m_N x}, \quad (\text{A.7})$$

$$\zeta = ixm_N\Delta z, \quad (\text{A.8})$$

$$t = \frac{B}{\tilde{b}^2}, \quad (\text{A.9})$$

$$u = t \cosh(\Omega\Delta z) + \sinh(\Omega\Delta z), \quad (\text{A.10})$$

$$w = (1 + t^2) \sinh(\Omega\Delta z) + 2t \cosh(\Omega\Delta z), \quad (\text{A.11})$$

$$\tilde{b}^2 = (0.65 \text{ GeV})^2 + \alpha_G Q^2. \quad (\text{A.12})$$

The limits for the α_G -integration are $x \leq \alpha_G \leq 0.1$, with α_G being the momentum fraction of the gluon relative to its parent quark. We use a running coupling constant [59]

$$\alpha_s(Q^2) = \frac{4\pi}{9 \ln\left(\frac{Q^2 + 0.25 \text{ GeV}^2}{(200 \text{ MeV})^2}\right)} \quad (\text{A.13})$$

with freezing at low scales. In (A.3), the gluon-gluon-nucleon cross section is parameterized in the form

$$\sigma_{GG}^N(\rho, \tilde{x}) = C_{eff}(\tilde{x})\rho^2. \quad (\text{A.14})$$

Note that σ_{GG}^N is sampled at the energy $\tilde{x} = x/\alpha_G$. For $\alpha_G \rightarrow x$, \tilde{x} can become greater than 0.1 and the dipole formulation is no longer valid. To overcome this problem, we employ the prescription

$$\tilde{x} = \min(x/\alpha_G, 0.1). \quad (\text{A.15})$$

The parameter C_{eff} is then determined from the asymptotic condition

$$\begin{aligned}
& \frac{\int d^2 b d^2 \rho |\Psi_{qG}(\rho)|^2 \left(1 - \exp\left(-\frac{1}{2}C_{eff}(\tilde{x})\rho^2 T_A(b)\right)\right)}{\int d^2 \rho |\Psi_{qG}(\rho)|^2 C_{eff}(\tilde{x})\rho^2} \\
& = \frac{\int d^2 b d^2 \rho |\Psi_{qG}(\rho)|^2 \left(1 - \exp\left(-\frac{9}{8}\sigma_{q\bar{q}}^N(\rho, \tilde{x}) T_A(b)\right)\right)}{\int d^2 \rho |\Psi_{qG}(\rho)|^2 \frac{9}{4}\sigma_{q\bar{q}}^N(\rho, \tilde{x})}, \quad (\text{A.16})
\end{aligned}$$

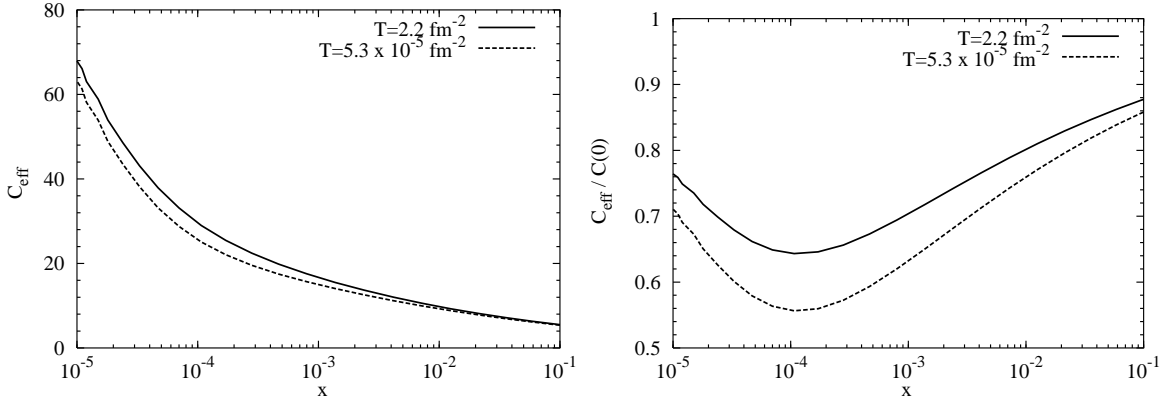


Figure 17: *The x -dependence of C_{eff} for gold at $Q^2 = 20 \text{ GeV}^2$. It is also shown how much C_{eff} is suppressed compared to $C(\rho = 0)$. The two curves in each plot correspond to impact parameter $b = 0$ (solid) and very large impact parameter (dashed), respectively.*

where $\sigma_{q\bar{q}}^N(\rho, \tilde{x})$ is the dipole cross section in the saturation model of [17]. The LC wave function for radiation of a quark from a gluon, including the nonperturbative interaction introduced in [29], reads

$$|\Psi_{qG}(\rho)|^2 = \frac{4\alpha_s}{3\pi^2} \frac{\exp(-\tilde{b}^2 \rho^2)}{\rho^2}. \quad (\text{A.17})$$

The choice of C_{eff} differs from the one made in [29], where $C(\rho = 0) = d\sigma_{GG}^N(\rho)/d\rho^2|_{\rho=0}$ was employed as the effective C. The prescription (A.16) is more realistic, because the C_{eff} is determined by those values of ρ which are most important for shadowing. Since the dipole cross section levels off at large separations, C_{eff} will be lower than $C(\rho = 0)$. This is illustrated in fig. 17. The $\sigma_L^{\gamma^*p}$ in the denominator of (A.2) is calculated with $C_{eff}(x)$ (instead of \tilde{x}).

With a constant nuclear density ρ_A , one can integrate (A.2) twice by parts,

$$\Delta\sigma_L^{\gamma^*A}(x, Q^2) = \frac{\pi}{12}\rho_A^2 \int_0^{2R_A} dL (L^3 - 12R_A^2L + 16R_A^3) \Gamma(x, Q^2, L), \quad (\text{A.18})$$

with $L = 2\sqrt{R_A^2 - b^2}$.

The $q\bar{q}$ -nucleus cross section in the long coherence time limit is calculated from the formula

$$\sigma_{q\bar{q}}^A(\rho, x) = 2 \int d^2b \left\{ 1 - \left(1 - \frac{\sigma_{q\bar{q}}^N(\rho, x) T_A(b) R_G(x, Q^2, b)}{2A} \right)^A \right\}, \quad (\text{A.19})$$

where gluon shadowing as function of impact parameter b is given by

$$R_G(x, Q^2, b) = 1 - \frac{\Delta\sigma_L^{\gamma^*A}(x, Q^2, b)}{T_A(b)\sigma_L^{\gamma^*p}(x, Q^2)}, \quad (\text{A.20})$$

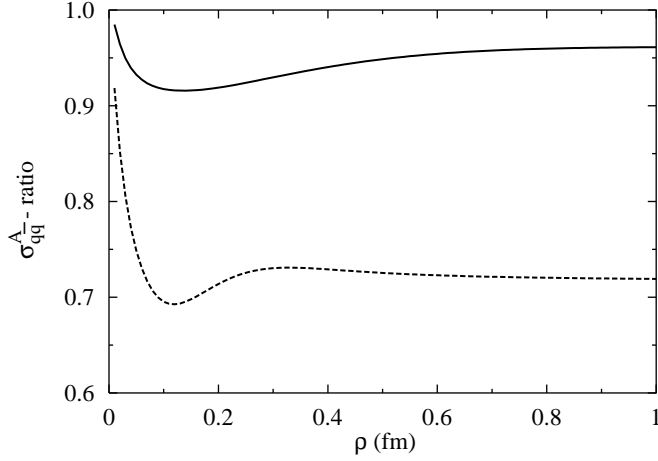


Figure 18: *This figure illustrates the influence of gluon shadowing on the $q\bar{q}$ -nucleus cross section. It shows the $q\bar{q}$ -nucleus cross section for gold calculated with gluon shadowing, Eq. (A.19), divided by the corresponding quantity without gluon shadowing, i.e. $R_G \rightarrow 1$. The solid curve is for $x = 10^{-3}$ (RHIC), while the dashed curve is for $x = 10^{-6}$ (LHC).*

and

$$\Delta\sigma_L^{\gamma^*A}(x, Q^2, b) = \rho_A^2 \int_0^L dz (L-z) \Gamma(x, Q^2, z), \quad (\text{A.21})$$

Furthermore, in (A.19) R_G is evaluated at the scale

$$Q^2 = \frac{1}{\rho^2} + 4 \text{ GeV}^2. \quad (\text{A.22})$$

Appendix B Calculation of the DY transverse momentum distribution

The differential DY cross section is expressed as a four-fold Fourier integral (17)

$$\begin{aligned} \frac{d\sigma(qp \rightarrow \gamma^* X)}{d \ln \alpha d^2 q_T} &= \frac{1}{(2\pi)^2} \int d^2 \rho_1 d^2 \rho_2 \exp[i\vec{q}_T \cdot (\vec{\rho}_1 - \vec{\rho}_2)] \Psi_{\gamma^*q}^*(\alpha, \vec{\rho}_1) \Psi_{\gamma^*q}(\alpha, \vec{\rho}_2) \\ &\times \frac{1}{2} \left\{ \sigma_{q\bar{q}}^N(\alpha\rho_1) + \sigma_{q\bar{q}}^N(\alpha\rho_2) - \sigma_{q\bar{q}}^N(\alpha(\vec{\rho}_1 - \vec{\rho}_2)) \right\}, \end{aligned} \quad (\text{B.1})$$

where

$$\begin{aligned} \Psi_{\gamma^*q}^{*T}(\alpha, \vec{\rho}_1) \Psi_{\gamma^*q}^T(\alpha, \vec{\rho}_2) &= \frac{\alpha_{em}}{2\pi^2} \left\{ m_f^2 \alpha^4 K_0(\eta\rho_1) K_0(\eta\rho_2) \right. \\ &\quad \left. + [1 + (1-\alpha)^2] \eta^2 \frac{\vec{\rho}_1 \cdot \vec{\rho}_2}{\rho_1 \rho_2} K_1(\eta\rho_1) K_1(\eta\rho_2) \right\}, \end{aligned} \quad (\text{B.2})$$

$$\Psi_{\gamma^*q}^{*L}(\alpha, \vec{\rho}_1) \Psi_{\gamma^*q}^L(\alpha, \vec{\rho}_2) = \frac{\alpha_{em}}{\pi^2} M^2 (1-\alpha)^2 K_0(\eta\rho_1) K_0(\eta\rho_2). \quad (\text{B.3})$$

and $\eta^2 = (1-\alpha)M^2 + \alpha^2 m_q^2$. The Fourier-integral is inconvenient for numerical calculations, but one can perform three of the integrations analytically for arbitrary $\sigma_{q\bar{q}}^N(\alpha\rho)$.

Consider the K_0 -part first. With help of the relation

$$K_0(\eta\rho) = \frac{1}{2\pi} \int d^2l \frac{e^{i\vec{l}\cdot\vec{\rho}}}{l^2 + \eta^2}, \quad (\text{B.4})$$

one finds

$$\begin{aligned} \left. \frac{d\sigma(qp \rightarrow \gamma^* X)}{d \ln \alpha d^2 q_T} \right|_{K_0\text{-part}} &= \frac{\alpha_{em}}{2\pi^2} [m_f^2 \alpha^4 + 2M^2 (1 - \alpha)^2] \frac{1}{(2\pi)^2} \int d^2\rho_1 d^2\rho_2 \frac{d^2l_1}{2\pi} \frac{d^2l_2}{2\pi} \\ &\times \frac{e^{i\vec{q}_T \cdot (\vec{\rho}_1 - \vec{\rho}_2)} e^{-i\vec{l}_1 \cdot \vec{\rho}_1} e^{i\vec{l}_2 \cdot \vec{\rho}_2}}{(l_1^2 + \eta^2) (l_2^2 + \eta^2)} \\ &\times \frac{1}{2} \{ \sigma_{q\bar{q}}^N(\alpha\rho_1) + \sigma_{q\bar{q}}^N(\alpha\rho_2) - \sigma_{q\bar{q}}^N(\alpha(\vec{\rho}_1 - \vec{\rho}_2)) \}. \end{aligned} \quad (\text{B.5})$$

Note that the term in the curly brackets consists of three contributions, which depend either only on ρ_1 or on ρ_2 or on the difference $\vec{\rho}_1 - \vec{\rho}_2$. Thus, the integral (B.5) can be split into three terms. In the integral that arises from the $\sigma_{q\bar{q}}^N(\alpha\rho_1)$ part, the ρ_2 -integration is trivially performed and leads to a two dimensional delta-function $\delta^{(2)}(\vec{q}_T - \vec{l}_2)$. This makes it possible to perform also the l_2 integration. The integration over l_1 gives just the MacDonald function K_0 (B.4). Thus one is left with a two-fold integration over ρ_1 . Provided the dipole cross section depends only on the modulus of ρ , one can use the relation

$$J_0 = \frac{1}{2\pi} \int d\phi e^{i\vec{l}\cdot\vec{\rho}} \quad (\text{B.6})$$

to perform one more integration. Here, J_0 is a Bessel function of first kind. The contribution arising from $\sigma_{q\bar{q}}^N(\alpha\rho_2)$ is calculated in exactly the same way. For the $\sigma_{q\bar{q}}^N(\alpha(\vec{\rho}_1 - \vec{\rho}_2))$ -part one has to introduce the auxiliary variable $\vec{d} = \vec{\rho}_1 - \vec{\rho}_2$, before the procedure described above can be applied.

The K_1 part is calculated in a similar way. Note that

$$K_1(\eta\rho) = -\frac{1}{\eta} \frac{d}{d\rho} K_0(\eta\rho). \quad (\text{B.7})$$

The K_1 -part reads

$$\begin{aligned} \left. \frac{d\sigma(qp \rightarrow \gamma^* X)}{d \ln \alpha d^2 q_T} \right|_{K_1\text{-part}} &= \frac{\alpha_{em}}{2\pi^2} [1 + (1 - \alpha)^2] \frac{1}{(2\pi)^2} \int d^2\rho_1 d^2\rho_2 \frac{d^2l_1}{2\pi} \frac{d^2l_2}{2\pi} \\ &\times \frac{e^{i\vec{q}_T \cdot (\vec{\rho}_1 - \vec{\rho}_2)} e^{-i\vec{l}_1 \cdot \vec{\rho}_1} e^{i\vec{l}_2 \cdot \vec{\rho}_2}}{(l_1^2 + \eta^2) (l_2^2 + \eta^2)} \vec{l}_1 \cdot \vec{l}_2 \\ &\times \frac{1}{2} \{ \sigma_{q\bar{q}}^N(\alpha\rho_1) + \sigma_{q\bar{q}}^N(\alpha\rho_2) - \sigma_{q\bar{q}}^N(\alpha(\vec{\rho}_1 - \vec{\rho}_2)) \}. \end{aligned} \quad (\text{B.8})$$

Like the K_0 -part, the complete integral (B.8) is split into three pieces, corresponding to the three terms in the curly brackets. Again, one integration over ρ is immediately performed,

leading to δ -functions, which allows one to do one integration over l . With the second l -integration, one recovers the MacDonald function K_1 via (B.7). For the K_1 -part, one also needs the relation

$$J_1(z) = -\frac{d}{dz}J_0(z). \quad (\text{B.9})$$

Although the calculation is slightly more cumbersome for the $\sigma_{q\bar{q}}^N(\alpha(\vec{\rho}_1 - \vec{\rho}_2))$ -part, all calculations are easily performed.

Finally, one finds

$$\begin{aligned} \frac{d\sigma(qp \rightarrow \gamma^* X)}{d \ln \alpha d^2 q_T} &= \frac{\alpha_{em}}{2\pi^2} \left\{ [m_f^2 \alpha^4 + 2M^2 (1 - \alpha)^2] \left[\frac{1}{q_T^2 + \eta^2} \mathcal{I}_1 - \frac{1}{4\eta} \mathcal{I}_2 \right] \right. \\ &+ \left. [1 + (1 - \alpha)^2] \left[\frac{\eta q_T}{q_T^2 + \eta^2} \mathcal{I}_3 - \frac{\mathcal{I}_1}{2} + \frac{\eta}{4} \mathcal{I}_2 \right] \right\}, \end{aligned} \quad (\text{B.10})$$

with

$$\mathcal{I}_1 = \int_0^\infty dr r J_0(q_T r) K_0(\eta r) \sigma_{q\bar{q}}^N(\alpha r) \quad (\text{B.11})$$

$$\mathcal{I}_2 = \int_0^\infty dr r^2 J_0(q_T r) K_1(\eta r) \sigma_{q\bar{q}}^N(\alpha r) \quad (\text{B.12})$$

$$\mathcal{I}_3 = \int_0^\infty dr r J_1(q_T r) K_1(\eta r) \sigma_{q\bar{q}}^N(\alpha r). \quad (\text{B.13})$$

The remaining integrals are evaluated numerically with the Numerical Recipes [60] routines.

References

- [1] D. M. Alde *et al.*, Phys. Rev. Lett. **64**, 2479 (1990).
- [2] M. B. Johnson *et al.* [FNAL E772 Collaboration], Phys. Rev. Lett. **86**, 4483 (2001) [hep-ex/0010051].
- [3] M. B. Johnson *et al.*, Phys. Rev. C **65**, 025203 (2002) [hep-ph/0105195].
- [4] K. J. Eskola, V. J. Kolhinen and P. V. Ruuskanen, Nucl. Phys. B **535**, 351 (1998) [hep-ph/9802350]; K. J. Eskola, V. J. Kolhinen and C. A. Salgado, Eur. Phys. J. C **9**, 61 (1999) [hep-ph/9807297].
- [5] L. V. Gribov, E. M. Levin and M. G. Ryskin, Nucl. Phys. B **188**, 555 (1981); Phys. Rept. **100**, 1 (1983).
- [6] P. L. McGaughey, J. M. Moss and J. C. Peng, Ann. Rev. Nucl. Part. Sci. **49**, 217 (1999) [hep-ph/9905409].

- [7] M. Luo, J. w. Qiu and G. Sterman, Phys. Rev. D **49**, 4493 (1994); Phys. Rev. D **50**, 1951 (1994); X. f. Guo, X. f. Zhang and W. Zhu, Phys. Lett. B **476**, 316 (2000) [arXiv:hep-ph/9911322].
- [8] K. J. Eskola, V. J. Kolhinen, P. V. Ruuskanen and R. L. Thews, hep-ph/0108093.
- [9] B. Z. Kopeliovich, proc. of the workshop Hirschegg '95: Dynamical Properties of Hadrons in Nuclear Matter, Hirschegg January 16-21, 1995, ed. by H. Feldmeyer and W. Nörenberg, Darmstadt, 1995, p. 102 (hep-ph/9609385).
- [10] S. D. Drell and T. Yan, Phys. Rev. Lett. **25**, 316 (1970) [Erratum-ibid. **25**, 902 (1970)].
- [11] S. J. Brodsky, A. Hebecker and E. Quack, Phys. Rev. D **55**, 2584 (1997) [hep-ph/9609384].
- [12] B. Z. Kopeliovich, A. Schäfer and A. V. Tarasov, Phys. Rev. C **59**, 1609 (1999), extended version in hep-ph/9808378.
- [13] B. Z. Kopeliovich, J. Raufeisen and A. V. Tarasov, Phys. Lett. B **503**, 91 (2001) [hep-ph/0012035]; J. Raufeisen, J. C. Peng and G. C. Nayak, Phys. Rev. D **66**, 034024 (2002) [arXiv:hep-ph/0204095].
- [14] B. Z. Kopeliovich, J. Raufeisen and A. V. Tarasov, “The color dipole approach to the Drell-Yan process in pA collisions,” hep-ph/0104155.
- [15] S. J. Brodsky, H. C. Pauli and S. S. Pinsky, Phys. Rept. **301**, 299 (1998) [arXiv:hep-ph/9705477].
- [16] A. B. Zamolodchikov, B. Z. Kopeliovich and L. I. Lapidus, JETP Lett. **33**, 595 (1981) [Pisma Zh. Eksp. Teor. Fiz. **33**, 612 (1981)].
- [17] K. Golec-Biernat and M. Wüsthoff, Phys. Rev. D **59**, 014017 (1999) [hep-ph/9807513]; Phys. Rev. D **60**, 114023 (1999) [hep-ph/9903358].
- [18] M. B. Johnson, B. Z. Kopeliovich and A. V. Tarasov, Phys. Rev. C **63**, 035203 (2001) [hep-ph/0006326].
- [19] G. T. Bodwin, S. J. Brodsky and G. P. Lepage, Phys. Rev. D **39**, 3287 (1989).
- [20] G. Bertsch, S. J. Brodsky, A. S. Goldhaber and J. F. Gunion, Phys. Rev. Lett. **47**, 297 (1981).
- [21] C. S. Lam and W.-K. Tung, Phys. Rev. D **18**, 2447 (1978); Phys. Rev. D **21**, 2712 (1980).
- [22] R. J. Glauber “High Energy Collision theory” in *Lectures in Theoretical Physics*, vol. 1, W. E. Brittin and L. G. Duham (eds.) Interscience, New York, 1959.

- [23] Y. V. Kovchegov and A. H. Mueller, Nucl. Phys. B **529**, 451 (1998) [arXiv:hep-ph/9802440].
- [24] S. J. Brodsky, P. Hoyer, N. Marchal, S. Peigne and F. Sannino, Phys. Rev. D **65**, 114025 (2002) [arXiv:hep-ph/0104291].
- [25] U. A. Wiedemann, Nucl. Phys. B **582**, 409 (2000) [arXiv:hep-ph/0003021].
- [26] A. H. Mueller, Nucl. Phys. B **335**, 115 (1990); Nucl. Phys. B **558**, 285 (1999) [hep-ph/9904404].
- [27] O. V. Kancheli, Print-75-0378 (TBILISI) In **Caneschi, L. (ed.): Regge theory of low-p(T) hadronic interactions** 312-315. (JETP Lett. 18 (1973) 274-277). (Pisma Zh. Eksp. Teor. Fiz. 18 (1973) 465-469). (see Book Index).
- [28] B. Blättel, G. Baym, L. L. Frankfurt and M. Strikman, Phys. Rev. Lett. **70**, 896 (1993); L. Frankfurt, A. Radyushkin and M. Strikman, Phys. Rev. D **55**, 98 (1997) [arXiv:hep-ph/9610274].
- [29] B. Z. Kopeliovich, A. Schäfer and A. V. Tarasov, Phys. Rev. D **62**, 054022 (2000) [hep-ph/9908245].
- [30] A. L. Ayala, M. B. Gay Ducati and E. M. Levin, Nucl. Phys. B **493**, 305 (1997) [hep-ph/9604383].
- [31] B. Kopeliovich, A. Tarasov and J. Hüfner, Nucl. Phys. A **696**, 669 (2001) [hep-ph/0104256].
- [32] B. Z. Kopeliovich, J. Nemchik, A. Schäfer and A. V. Tarasov, Phys. Rev. C **65**, 035201 (2002) [hep-ph/0107227].
- [33] V. N. Gribov, Sov. Phys. JETP **29**, 483 (1969) [Zh. Eksp. Teor. Fiz. **56**, 892 (1969)]; Sov. Phys. JETP **30**, 709 (1970) [Zh. Eksp. Teor. Fiz. **57**, 1306 (1970)].
- [34] I. Balitsky, Nucl. Phys. B **463**, 99 (1996) [arXiv:hep-ph/9509348]. Y. V. Kovchegov, Phys. Rev. D **60**, 034008 (1999) [arXiv:hep-ph/9901281].
- [35] C. W. De Jager, H. De Vries and C. De Vries, Atom. Data Nucl. Data Tabl. **36**, 495 (1987).
- [36] T. Schäfer and E. V. Shuryak, Rev. Mod. Phys. **70**, 323 (1998) [hep-ph/9610451].
- [37] V. M. Braun, P. Górnicki, L. Mankiewicz and A. Schäfer, Phys. Lett. B **302**, 291 (1993).
- [38] M. D'Elia, A. Di Giacomo and E. Meggiolaro, Phys. Lett. B **408**, 315 (1997) [hep-lat/9705032].
- [39] B. Z. Kopeliovich, J. Raufeisen and A. V. Tarasov, Phys. Rev. C **62**, 035204 (2000) [hep-ph/0003136].

- [40] H. L. Lai *et al.* [CTEQ Collaboration], *Eur. Phys. J. C* **12**, 375 (2000) [hep-ph/9903282].
- [41] H. Plathow-Besch, “The Parton distribution function library,” *Int. J. Mod. Phys. A* **10**, 2901 (1995); “PDFLIB: Proton, Pion and Photon Parton Density Functions, Parton Density Functions of the Nucleus and α_s Calculations”, User’s Manual - Version 8.04, W5051 PDFLIB, 2000.04.17, CERN-PPE.
- [42] J. Raufeisen, Ph.D. thesis “QCD coherence effects in high energy reactions with nuclei,” hep-ph/0009358.
- [43] A. Drees, *Nucl. Phys. A* **698**, 331 (2002) [nucl-ex/0105019].
- [44] B.Z. Kopeliovich and F. Niedermayer, *Nuclear screening in J/Ψ and Drell-Yan pair production*, JINR-E2-84-834, Dubna 1984, a scanned version in KEK library: http://www-lib.kek.jp/cgi-bin/img_index?8504113.
- [45] J.-C. Peng, private communication.
- [46] D. M. Alde *et al.*, *Phys. Rev. Lett.* **66**, 2285 (1991).
- [47] D. M. Kaplan *et al.*, *Phys. Rev. Lett.* **40**, 435 (1978).
- [48] L. D. McLerran and R. Venugopalan, *Phys. Rev. D* **49**, 2233 (1994) [hep-ph/9309289]; *Phys. Rev. D* **49**, 3352 (1994) [hep-ph/9311205]; *Phys. Rev. D* **50**, 2225 (1994) [hep-ph/9402335].
- [49] J. Dolejši, J. Hüfner and B. Z. Kopeliovich, *Phys. Lett. B* **312**, 235 (1993) [hep-ph/9305238].
- [50] E. Mirkes, *Nucl. Phys. B* **387**, 3 (1992); A. Brandenburg, O. Nachtmann and E. Mirkes, *Z. Phys. C* **60**, 697 (1993).
- [51] S. Falciano *et al.* [NA10 Collaboration], *Z. Phys. C* **31**, 513 (1986); J. S. Conway *et al.*, *Phys. Rev. D* **39**, 92 (1989).
- [52] R. J. Fries, A. Schäfer, E. Stein and B. Müller, *Nucl. Phys. B* **582**, 537 (2000) [hep-ph/0002074]; R. J. Fries, B. Müller, A. Schäfer and E. Stein, *Phys. Rev. Lett.* **83**, 4261 (1999) [hep-ph/9907567].
- [53] J. C. Collins, D. E. Soper and G. Sterman, *Nucl. Phys. B* **250**, 199 (1985).
- [54] M. C. Abreu *et al.* [NA50 Collaboration], *Phys. Lett. B* **410**, 337 (1997).
- [55] J. C. Peng *et al.* [E866/NuSea Collaboration], *Phys. Rev. D* **58**, 092004 (1998) [hep-ph/9804288].
- [56] B. Z. Kopeliovich, J. Raufeisen and A. V. Tarasov, *Phys. Lett. B* **440**, 151 (1998) [hep-ph/9807211]; J. Raufeisen, A. V. Tarasov and O. O. Voskresenskaya, *Eur. Phys. J. A* **5**, 173 (1999) [hep-ph/9812398].

- [57] M. Arneodo, Phys. Rept. **240**, 301 (1994).
- [58] M. Glück, E. Reya and A. Vogt, Eur. Phys. J. C **5**, 461 (1998) [hep-ph/9806404].
- [59] Y. L. Dokshitzer, G. Marchesini and B. R. Webber, Nucl. Phys. B **469**, 93 (1996) [hep-ph/9512336].
- [60] W. H. Press, S. A. Teukolsky, W. T. Vetterling and B. P. Flannery, “Numerical Recipes in C”, 2nd edition, Cambridge University Press, New York, 1995.